A QUEST

FOR NEUTRAL-CURRENT-ENHANCED

PARITY MIXING

IN ^{18}F

Thesis by

Michael Murdock Lowry

In Partial Fulfillment of the Requirements

for the Degree of

Doctor of Philosophy

California Institute of Technology

Pasadena, California

1979

(Submitted July 21, 1978)

ACKNOWLEDGMENTS

It is a pleasure to acknowledge the helpful and stimulating atmosphere provided by the students, faculty, and staff of Kellogg Radiation Laboratory. I am deeply grateful to Professor C. A. Barnes without whose guidance, encouragement and calm diplomacy this work would not have been possible. Special thanks are due Professor E. G. Adelberger, who suggested and began the experiment and who enthusiastically supported its completion. Thanks are also due the other collaborators who have devoted so much time and effort: Dr. J. M. Davidson, Dr. R. E. Marrs, and Prof. F. B. Morinigo. In addition, contributions from Dr. H. E. Swanson, Prof. B. Chang, Prof. H. Winkler, and Dr. P. Ingalls are gratefully acknowledged.

Thanks are extended to the students and staff of the California State University, Los Angeles, Physics Department who spent many hours operating the Van de Graaff accelerator: D. Brown, L. Gin, C. Malone, C. Sato, D. Scott, and especially W. Davis whose maintenance and repair of the accelerator were instrumental in carrying out this measurement.

The California State, Los Angeles, Van de Graaff accelerator laboratory is operated with State of California funds. Financial assistance was granted by the National Science Foundation (Contract No. PHY76-83685), by the U.S. Energy Research and Development Administration (Contract No. EY-77-C-06-1388), by the National Science Foundation Trainee program, by the Millikan Fellowship Fund, and by the Alfred P. Sloan Foundation.

ABSTRACT

A measurement of the circular polarization of the gamma rays from the 1.081-MeV-to-0.0-MeV transition of the nucleus ^{18}F has been made in order to search for possible effects of neutral weak currents. Excited ^{18}F nuclei were created in a flowing water target by a 4.0 MeV ^{3}He beam via the reaction $^{16}O(^{3}He,p)^{18}F^{*}$. Pulse-height spectra were accumulated for approximately 1500 hours of running time in two Ge(Li) detectors which viewed the target through transmission-style Compton polarimeters. Additional measurements were made to calibrate and check the apparatus. A careful analysis of the data leads to a 1.081 MeV gamma ray circular polarization of $(-0.7 \pm 2.0) \times 10^{-3}$. This value is consistent with zero, and smaller than but not inconsistent with the most recent predictions based on the Weinberg-Salam theory of neutral currents.

TABLE OF CONTENTS

I. INTRODUCTION

The discovery of muon-less neutrino-induced events at Cern (Hasert et al. 1973) and at Fermilab (Benvenuti et al. 1974) necessitates a major revision of the theory of weak interactions as originally proposed by Feynman and Gell-Mann (1958) and subsequently modified by Cabibbo (1963). Whereas the Cabibbo model for weak interactions envisioned the interaction occurring only between two particle currents, both of which changed their total charge by one unit, this new phenomenon clearly requires a neutrino-in, neutrino-out current which manifestly does not modify its charge. Just such neutral currents had been predicted as a consequence of attempts to unify the weak and electromagnetic forces in a renormalizable fashion. In particular, the model of Weinberg (1967) and Salam (1968) provided a simple, one-parameter explanation of these events.

At the same time as the neutrino experiments were being performed, remarkable new results were being obtained in nuclear parity-violation experiments, and these experiments called attention once again to the possibility of studying fundamental facets of the weak interaction in such experiments. Lobashov et al. (1972) reported a circular polarization of $P_\gamma = (-1.30 \pm 0.45) \times 10^{-6}$ for the photon in thermal neutron-proton capture. The parity-forbidden alpha decay of the 2^- state at 8.88 MeV in ^{16}O was observed by Neubeck et al. (1974) to occur with a width $\Gamma = (1.03 \pm 0.28) \times 10^{-10}$ eV. In the nucleus ^{19}F, the parity-nonconserving angular distribution asymmetry of the 110 keV gamma ray transition from the (polarized) first excited state ($J^P = \frac{1}{2}^-$) to the

ground state ($J^P = \frac{1^+}{2}$), $A_\gamma = (-1.8 \pm 0.9) \times 10^{-4}$, was measured by Adelberger et al. (1975). All of these cases (as well as earlier experiments; see Gari 1973 for a review of earlier results) are either insensitive to the isovector component of the weak interaction or do not differentiate between the isovector and the isoscalar or isotensor components.*

Two states, of spin zero, opposite parity, and isospin zero and one, less than 40 keV apart, make the ^{18}F nucleus an ideal candidate for a study of the isovector portion of the parity-nonconserving weak interaction. A prediction by Gari et al. (1975) of a circular polarization, $P_\gamma = 5.7 \times 10^{-3}$, for the 1.08 MeV de-excitation gamma ray from one of those states, derived on the basis of the enhancement of the weak potential calculated by Gari and Reid (1974) from the Weinberg-Salam theory, appeared within the reach of experimental verification. Chapter II of this thesis describes the calculations underlying the Gari et al. prediction and other predictions. In Chapter III, the experimental apparatus and procedure developed to carry out the measurements are described. The experimental results are presented and compared with the theoretical predictions in Chapter IV. Various calibration and test measurements made on the apparatus are outlined in Chapter V.

---

*A compilation of parity-violation experiments to date is given in the Supplementary Table, page 97.

II. THEORY

The process of predicting a parity-violating nuclear effect can be divided into three pieces: 1) a basic particle-particle interaction must be assumed, 2) this interaction must be translated into a nucleon-nucleon potential, and 3) the effects of this potential must be calculated for the nucleus of interest.

A. Theory of the Basic Interaction

The conventional theory of weak interactions or charged current (c.c.) model is basically that of Feynman and Gell-Mann (1958) with modifications by Cabibbo (1963). In this model, the weak Hamiltonian, H_w^{cc}, is the symmetric product of a current, J, times its Hermitian conjugate,

$$H_w^{cc} = \frac{G}{2\sqrt{2}} [J^*J + JJ^*] \quad ,$$

where J is the sum of a strangeness-conserving hadronic current, a strangeness-changing hadronic current, a leptonic current, and, if we include the GIM mechanism (Glashow, Iliopoulos, and Maiani 1970), a charm-changing hadronic current. To more clearly illustrate the features of this model, we will use a quark representation for the current with (u,d,s,c) = (up quark, down quark, strange quark, charm quark). The hadronic current becomes

$$J^{cc} = \bar{u}\gamma(1 - \gamma_5)(d \cos \theta_c + s \sin \theta_c) + \bar{c}\gamma(1 - \gamma_5)(-d \sin \theta_c + s \cos \theta_c),$$

where θ_c is the Cabibbo angle $\sim 13°$. The charm quark is expected to be so heavy that its contribution to the quark-antiquark sea within the nucleon is quite small and its propagation as a virtual particle negligible; thus it is assumed that we can safely drop the second half of J^{cc} from

consideration in the nucleon-nucleon interaction. The term $\bar{u}d$ is a component of an isovector with $\Delta S = 0$, and the term $\bar{u}s$ is an isospinor with $\Delta S = 1$. The factor γ is a vector (V) and $\gamma\gamma_5$ is an axial vector (A); therefore, we can rewrite the hadronic current as

$$J^{cc} = \cos\theta_c(V^{\Delta S=0}_{I=1} - A^{\Delta S=0}_{I=1}) + \sin\theta_c(V^{\Delta S=1}_{I=1/2} - A^{\Delta S=1}_{I=1/2}) \quad .$$

If this current is substituted back into the Hamiltonian and only the strangeness conserving, parity-nonconserving terms are retained, we obtain

$$H_w^{cc}(PNC) = \frac{G}{2\sqrt{2}}[\cos^2\theta_c(-2V^{\Delta S=0*}_{I=1}\ A^{\Delta S=0}_{I=1} + \text{Hermitian conjugate})$$

$$+ \sin^2\theta_c(-2V^{\Delta S=1*}_{I=1/2}\ A^{\Delta S=1}_{I=1/2} + \text{Hermitian conjugate})] \quad .$$

The term proportional to $\cos^2\theta_c$, which is an isovector crossed into an isovector, would have pieces which transform as I = 0,1, and 2, except that the isovector piece is cancelled by the symmetry introduced by including the Hermitian conjugate, leaving only the isoscalar and isotensor parts. The $\sin^2\theta_c$ term will, similarly, have only the isovector piece and no isoscalar piece. Because $\sin^2\theta_c \simeq 1/20$ and an isovector interaction only appears in the term proportional to $\sin^2\theta_c$, the isovector potential is strongly suppressed in the conventional charged-current model of weak interactions.

This conventional model cannot explain the neutral current events observed in the high energy neutrino experiments. Of the models that explain the observed neutral current effects, one of the most appealing is that of Weinberg (1967) and Salam (1968). This model is a gauge

theory based on an SU(2) × U(1) symmetry group which attempts to unify electromagnetic and weak phenomena. It utilizes the Higgs mechanism to give mass to three vector meson mediators of the weak interaction, $W^{\pm}$ and Z^{o}, while maintaining a zero mass for the photon and retaining renormalizability. The Hamiltonian for this theory when extended to hadrons (Weinberg 1972) is of the same form as in the charged-current case except that the current J is augmented by the addition of the new neutral current,

$$J^{nc} = \frac{1}{2}\bar{u}\gamma(1-\gamma_5)u - \frac{1}{2}\bar{d}\gamma(1-\gamma_5)d + \frac{1}{2}\bar{c}\gamma_\mu(1-\gamma_5)c$$
$$- \frac{1}{2}\bar{s}\gamma(1-\gamma_5)s - 2\sin^2\theta_W J^{em} \quad ,$$

where the leptonic current has been omitted, θ_W is the Weinberg angle ($\sin^2\theta_W \sim .3$), and J^{em} is the electromagnetic current

$$J^{em} = \frac{2}{3}\bar{u}\gamma u - \frac{1}{3}\bar{d}\gamma\, d - \frac{1}{3}\bar{s}\gamma\, s + \frac{2}{3}\bar{c}\gamma\, c \quad ,$$

again ignoring leptonic terms. If the strange and charm terms are dropped and it is noted that $\frac{1}{2}(\bar{u}u-\bar{d}d)$ is isovector while $\frac{1}{2}(\bar{u}u+\bar{d}d)$ is isoscalar, the neutral current simplifies to:

$$J^{nc} = (1-2\sin^2\theta_W)V^{\Delta S=0}_{I=1} - A^{\Delta S=0}_{I=1} - \frac{2}{3}\sin^2\theta_W\, V^{\Delta S=0}_{I=0} \quad .$$

Thus, the parity-violating weak Hamiltonian receives additional terms which are the symmetric product of two isovectors ($\Delta I=0,2$ terms) and the product of an isoscalar and an isovector, implying an isovector term, $-\frac{2}{3}\sin^2\theta_W(-2V^{\Delta S=0*}_{I=0}A^{\Delta S=0}_{I=1} + \text{h.c.})$. Thus, we would naively expect the

isovector, parity-nonconserving potential to be modified by a factor, $1 - \frac{2 \sin^2\theta_W}{3 \sin^2\theta_c} \simeq -3$. This ignores the difference between the two sets of V·A operators. To take this into account requires a dynamic calculation of the quarks within the nucleons or some assumptions about the symmetry rules these quarks obey. By utilizing the latter approach, Gari and Reid (1974) obtained an enhancement of sixteen. It was on the basis of the Gari and Reid enhancement that the Gari et al. (1975) calculation of the circular polarization in the nucleus ^{18}F was made, and the present experiment undertaken.

A more complete treatment of the problem, in which the quark natures of the operators are explicitly treated by reference to dynamical calculations, was given by Donoghue (1976). He found that the isovector potential was enhanced over the conventional theory by approximately a factor of three, but the charged current isovector potential arising from the strangeness-changing current was zero, and the only contribution was from the isospin breaking in the $\cos^2\theta_c$ term from the proton-neutron mass difference. This last result had been obtained earlier in the works of Schülke (1972) and Körner (1973). The discrepancy in the charged-current results appears to invalidate the assumption of octet dominance used to derive the conventional result from the strangeness-changing, nonleptonic hyperon decay amplitudes, but the primitive nature of the quark calculations may make this judgment premature.

Desplanques and Micheli (1977) have investigated the effect of the nucleon quark-antiquark sea as well as several procedures for dealing with deviations from SU(3) symmetry in hyperons, all in a Weinberg-Salam framework. They obtain a potential which is enhanced by a factor of about nine

over the conventional, charged-current results.

Many other models have been proposed for including neutral currents in the weak interaction. Unfortunately, no detailed calculation of the isovector, parity-nonconserving potential to be expected in those models has been carried out except for the old pre-neutrino experiment models (see Desplanques and Hadjimichael 1976, Gari 1973, and references cited therein), which have been ruled out experimentally, and certain new gauge theories which, by their construction, contain no parity violation (see Hung and Sakurai 1977, Galić and Tadić 1976, and references cited therein).

B. The Nucleon-Nucleon, Isovector, Parity-Nonconserving Potential

The isovector, parity-violating potential is conventionally viewed as arising from the exchange of a pion between two nucleons where one of the interaction vertices is mediated by the strong interaction, and the other proceeds via the weak, parity-violating interaction. It is beyond the scope of this thesis to derive this potential (see, for example, Fischbach and Tadić 1973), but we can present the result of the derivation and point out the sources of the various components of the potential,

$$V_{\pi NN} = \frac{g f}{16\pi M\sqrt{2}}\, i(\tau_1 \times \tau_2)^z\, (\vec{\sigma}_1 + \vec{\sigma}_2) \cdot [\vec{p}_1 - \vec{p}_2, \frac{e^{-mr_{12}}}{r_{12}}]$$

where g is the standard strong πNN coupling constant given by $g^2/4\pi = 14.4$; M is the nucleon mass; m is the pion mass, and f is the weak coupling constant, $f = |a(n^o_-)| = |a(p^+_+)|$, whose value depends on the model weak interaction being used. The conventional charged current value for f, adopted by Gari and Reid (1974), is $f = 4.5 \times 10^{-8}$. The unconventional

charged current number is $f \simeq 0.28 \times 10^{-8}$ (Donoghue 1976). As computed by Desplanques and Micheli (1977), the Weinberg-Salam model value is $f \simeq 4 \times 10^{-7}$.

The four operator factors in $V_{\pi NN}$ describe the isospin character, $i(\tau_1 \times \tau_2)^z$; the axial-vector character, $(\vec{\sigma}_1 + \vec{\sigma}_2)$; the vector character, $\vec{p}_1 - \vec{p}_2$; and the pion field dependence, [, $(e^{-mr_{12}})/r_{12}$] of the basic interaction. Any theory which achieves parity violation by V·A interaction will lead to the same operators in the πNN potential; the only effect of different models will be to modify the coupling constant, f, in front of the operators. Because the operator structure is unmodified from model to model, the nuclear structure calculation need only be carried out once; and the results can then be scaled for any desired coupling constant.

Unfortunately, this expression for the isovector, parity-nonconserving, nucleon-nucleon potential neglects contributions from two-pion exchange and ρ-meson exchange. Although of shorter range, both of these corrections may be significant. Calculations for the nucleus ^{41}K using the conventional, charged-current derivations indicated corrections of the order of 30% (see, for example, Pirner and Riska 1973 or Chemtob and Desplanques 1974). Since no calculation of these contributions in the new gauge theories exists, they are a source of some worry.

C. The ^{18}F Case

If we now turn to the specific case of the nucleus ^{18}F (Ajzenberg-Selove 1972), we find two states of the same spin and opposite parity separated by just 39 keV (see Figure 1). The upper spin-zero state,

located 1.081 MeV above the ground state, has odd parity and isospin zero. It decays exclusively to the ground state with a lifetime of $\tau_m = (30\pm3) \times 10^{-12}$ seconds via an isospin-forbidden electric dipole transition. The lower spin zero state has even parity and is the analog of the ^{18}O and ^{18}Ne ground states. Its strong magnetic dipole transition to the ground state has a measured lifetime of $\tau_m = (4^{+3}_{-2}) \times 10^{-15}$ seconds. Because this transition can be related to the ^{18}Ne and ^{18}F beta decays, the lifetime can be deduced from those ft values; this procedure yields almost the same result but with much tighter constraints.

The next spin-zero state is approximately 3.7 MeV higher; therefore to a good approximation we may treat the parity mixing between these two states as a simple, two-state perturbation problem. The resulting mixed wavefunctions, $|1.081\rangle$ and $|1.042\rangle$, in terms of the states of pure parity $|J^P = 0^-, T = 0\rangle$ and $|0^+,1\rangle$, are

$$|1.081\rangle = |0^-,0\rangle + \frac{\langle 0^+,1| H^{PNC}_{\Delta T=1} |0^-,0\rangle}{\Delta E} |0^+,1\rangle \quad ,$$

$$|1.042\rangle = |0^+,1\rangle - \frac{\langle 0^-,0| H^{PNC}_{\Delta T=1} |0^+,1\rangle}{\Delta E} |0^-,0\rangle \quad ,$$

where $\Delta E = 39$ keV is the energy separation between the two states, and $H^{PNC}_{\Delta T=1}$ is the isovector, parity-nonconserving potential.

If the electromagnetic decays of these two states to the ground state are now computed, terms arising from the interference between the electric and magnetic dipoles are produced. These cross terms result in circular polarizations P_γ in the emitted gamma rays which are simply equal to

$$P_\gamma(1.081) = -2 \frac{\mathrm{Re}\langle 0^+,1|H^{PNC}_{\Delta T=1}|0^-,0\rangle}{\Delta E} \frac{\langle M1\rangle}{\langle E1\rangle} \quad ,$$

$$P_\gamma(1.042) = 2 \frac{\mathrm{Re}\langle 0^+,1|H^{PNC}_{T-1}|0^-,0\rangle}{\Delta E} \frac{\langle E1\rangle}{\langle M1\rangle} \quad ,$$

where <E1> and <M1> denote the reduced matrix elements for the E1 and M1 decays of the pure states. The magnitude of the ratio of these two reduced matrix elements can be determined from the square root of the ratio of the lifetimes of the two states, $|\langle M1\rangle/\langle E1\rangle| = 87$. Thus the strength of the magnetic dipole transition greatly enhances the polarization of the 1.081 gamma ray, while suppressing that of the 1.042 gamma ray, which can, for purposes of this experiment, be considered to have no circular polarization.

To obtain a prediction for the circular polarization, one must calculate the matrix element of the charged current potential and then scale the polarization with one's choice of enhancement factor. Both of the spin zero states are relatively good shell model states, lying at low excitation in a light nucleus. The pion exchange interaction has a relatively long range and thus reduced sensitivity to the effects of nucleon hard cores and short-range correlations. Thus there are reasons to expect that the nuclear physics portion of the parity mixing calculations is reliable.

Presently three charged-current calculations exist in the literature. The earliest determination (Henley 1968) was an order of magnitude estimate ($P_\gamma \sim \pm 2 \times 10^{-5}$) made in a survey of likely candidate reactions for parity violation study. A more complete calculation by Wambach et al.

(1970) obtained an even smaller value of $P_\gamma = \pm 0.3 \times 10^{-5}$. The most recently published result (Gari et al. 1975) is significantly larger, $P_\gamma = \pm 3.6 \times 10^{-4}$. The large discrepancy between these last two values is explained by Gari (private communication) as due to an error in the earlier work. More recent, unpublished results (Gari 1977) are in qualitative agreement with this last value and somewhat larger ($\pm 4.5 \times 10^{-4}$).

Gari et al. (1975) used the enhancement of sixteen derived by Gari and Reid (1974) on the basis of the Weinberg-Salam model to obtain a prediction of $P_\gamma = \pm 5.7 \times 10^{-3}$ for the circular polarization of the 1.081 MeV gamma ray. A circular polarization of this magnitude appeared large enough to allow an experimental test of the prediction to be made.

Unfortunately, none of the calculations predicts the sign of the circular polarization. Desplanques and Micheli (1977) have given a definite prediction for the sign of the isovector, parity-violating potential within the Weinberg-Salam theory; the strength of the magnetic dipole clearly indicates that its sign would be given by even the most primitive calculation; only the strongly inhibited electric dipole transition could present a problem. Even there, the electric dipole strength clearly arises from the mixing with the giant dipole resonance so the sign should be determinable in a careful calculation. However, even with the sign uncertainty, it appeared that it should still be possible to confront the predicted magnitude of the circular polarization of the 1.081 MeV gamma ray with an experimentally determined number.

III. EXPERIMENTAL METHOD

Once the purpose of an experiment is specified, it is then necessary to set up a procedure for performing that experiment. That procedure is the subject of the following sections. They deal with the beam that creates the $^{18}F^*$'s, the transport of that beam to a target, the target where the fluorine is created, the circular polarimeters which act on the subsequent gamma rays, and the detection system for those gamma rays.

A. The Beam

Because lithium drifted germanium detectors were to be used, the number of neutrons produced had to be kept to a minimum. Of the five reactions which lead to $^{18}F^*$ below the energy at which the neutron exit channel of the compound nucleus opens up, only two proceed by particle exit channels, which make possible large cross sections. One of these is the reaction $^{21}Ne(p,\alpha)^{18}F$, but the cost of ^{21}Ne and the difficulty of working with gas targets argue against this reaction. The other is $^{16}O(^3He,p)^{18}F$, with a Q-value to the ground state of 2.0334 MeV, and this was the reaction chosen for the experiment.

The KN4000 Van de Graaff accelerator at the California State University, Los Angeles, provided 30 to 50 microamperes of singly-charged ^3He ions at an energy of 4 MeV. The ^3He energy was well below the neutron production threshold, which occurs at a beam energy of 3.795 MeV once the beam has traversed a 7500Å nickel foil, losing an energy of 286 keV. A description of the equipment between the accelerator and that foil follows.

B. The Fuzzer

After traversing the analyzing magnet, the beam passed through two copper apertures, each approximately 6 cm long and 0.8 cm in diameter. These two apertures are depicted on the upper left hand side of Figure 2. The region between them was pumped by a diffusion pump, and this combination served to isolate the vacuum of the accelerator and the analyzing magnet from the region downstream of the second aperture.

Argon gas was introduced into the latter region at a rate sufficient to cause the pressure above the diffusion pump to rise from a base vacuum of about 2×10^{-6} torr to a value of about 3.5×10^{-5} torr. Although no measurement was made of the actual pressure in the higher pressure section, an estimate of the aperture conductance and the pump speed suggests a pressure of about five microns for that section of the beam path. The beam exited this higher pressure region approximately three meters downstream from the diffusion pump through a 9 cm long, 0.55 cm diameter copper canal, which was covered on the upstream side by a tantalum aperture in order to prevent nuclear reactions between ^{3}He and copper. This tantalum aperture typically stopped sufficient beam during the experiment to glow white hot on its inner edge. The region downstream of this final canal was also pumped by a large diffusion pump; thus the beam passed through a three meter long, differentially-pumped argon gas target, at a pressure of about 5 microns.

The purpose of this gas target was to multiply scatter the beam particles sufficiently to prevent the accidental focussing of any portion of the beam spot into a small enough area to damage the ^{18}F producing target further downstream. Such unintentional focussing could result from

attempts to tune the beam by the accelerator operator, or from the more-or-less normal small variations in ion source emittance or in the accelerating tube potential distribution. As a result of this fuzzing of the beam by the argon gas target, the beam energy was degraded by about 2 keV, and the ^{3}He ions were stripped to charge two; a more significant result of the fuzzing was that more than half of the beam intensity was lost on collimators so that the target current was typically between 20 and 30 microamperes of doubly-charged beam.

Following the fuzzer, the beam passed through two solenoid-driven fast-closing vacuum valves whose operation will be discussed in connection with the target system. It then impinged on the beam-size defining aperture, which consisted of a tantalum annulus with an inner diameter of 0.32 cm attached to a copper disk. The copper disk was pierced near its outer edge by several large holes to improve pumping speed, mounted in a ceramic ring to isolate it from electrical ground, and cooled by flowing water. Typical good operation of the accelerator resulted in 15 to 25 microamperes of current intercepted by this aperture. Because such large amounts of beam were dumped on this aperture, and also on the final fuzzer aperture, extra care was taken to clean these apertures of carbon buildup, since carbon, via the $^{12}C(^{3}He,n)^{14}O$ reaction [Q = -1.148 MeV] was a principal source (usually the principal source) of neutrons.

Between the beam-defining aperture and the nickel foil which formed the beginning of the target, there were three more restrictions through which the beam had to pass. The first of these was a 0.95 cm diameter tube traversing a 7.6 cm long in-line cold trap maintained at liquid nitrogen temperature. Following that was a 0.40 cm diameter

opening, and finally, located just 3.0 cm upstream of the foil, there was a 0.44 cm diameter tantalum aperture. Both of these apertures served as protective devices rather than as collimators, since the beam could only strike them when the system was misaligned. Having threaded all of these obstacles, the beam then impinged on the nickel foil which formed the beginning of the target system.

C. The Target System

The choice of $^{16}O(^{3}He,p)^{18}F$ as the production reaction required development of a target which met three demands. First, in order to maximize the yield, a stopping thickness of material with as much of its stopping power in the form of oxygen as possible was necessary. Because the beam dumped approximately 50 watts of power into the target, cooling of the target was required. Finally, ^{18}F beta decays to ^{18}O with a half-life of about two hours and must therefore be largely removed from the target region to prevent the annihilation radiation from flooding the detectors. All of these criteria were met by a target of liquid water flowing past the beam, and sealed from the vacuum system by a thin nickel foil.

In this system, schematically shown in Figure 3, distilled water was siphoned from a 20 liter reservoir and then allowed to flow approximately 5 meters to a solenoid valve. Once past that valve, the water entered the bottom of the target cell. This cell was an aluminum chamber with a lucite back that was shaped to constrict the flow cross section just as the water passed in back of the nickel entrance foil, in order to obtain the highest velocity water flow across the nickel foil. In this way, the foil was cooled as efficiently as possible; and bubbles, pre-

sumably of hydrogen and oxygen arising from the dissociation of water by the beam, were swept away from the foil as rapidly as possible. From the top of the water cell, the water passed through a second solenoid valve, and thence to a peristaltic pump which propelled the water back to the reservoir.

The key to the success of this target system was the ability of the foil to support atmospheric pressure while under intense bombardment [approximately 3 watts of beam power were deposited in a 750 nanometer thick foil; thus, even though the beam was rather evenly diffused over a 0.32 cm diameter spot, the foil would quickly melt if contact with the cooling water behind it were lost]. The foils were commercially produced by the Chromium Corporation of America, Cleveland, Ohio, and were used in two thicknesses, 750 and 1000 nanometers. Because the thicker foils reduced the beam energy by a further 100 keV, and the accelerator was already operating at its maximum legal energy, the beam intensity had to be increased when the thicker foils were used, in order to maintain the same count rate. Unfortunately, this increase in beam current approximately cancelled the effect of the extra strength on the lifetime of the foil. Since the higher beam current also resulted in more neutrons being produced, the 750 nanometer foils were preferred.

In order to mount the foils, they were first cut into squares, 1.27 cm on a side, and then examined over an intense light source to determine the location of any pinholes. About one in four squares had to be rejected because of the presence of such pinholes. The foils were attached to stainless steel holders by plastic-to-metal epoxy (Epoxylite No. 8751). The epoxy was first applied to the holders in a thin layer. The

thickness of this layer proved to be crucial; if it was too thin, the foil would pull loose under vacuum; if itwas too thick, the foil's lifetime under beam bombardment was sharply reduced. [This last problem was never fully understood but may have been caused by the epoxy flowing out, before setting, onto the region of the foil to be bombarded by the beam. This would create a stopping thickness of material which would cause the foil to overheat and rupture.] The nickel foils were laid on the freshly applied epoxy layer, and the epoxy was then cured for at least six hours at a slightly elevated temperature. The foils were then ready for installation in the target system.

In addition to the mounting techniques, there were two other practices which seemed to extend the foil lifetimes. Careful centering and defocussing of the beam was important, and was made possible by the serendipitous discovery that the water under direct bombardment glowed with a bluish-white light. Thus the beam profile was directly observable through the plastic back of the water target cell. A second trick, of less certain effectiveness, was the introduction of the compound NiOH into the target water, by placing several grams of NiOH crystals into the water storage reservoir. This procedure was motivated by two observations: 1) that the foils appeared to grow thinner as they aged, since the count rate was observed to grow with time, and 2) that the foils had longer lifetimes with water that had undergone previous bombardment. These two facts are consistent with the hypothesis that normally insoluble nickel was being eaten away by the chemical action of the ions created by the passage of the beam, and that the presence of nickel ions in the water from previous bombardments would somewhat inhibit this process. Since

the target water had to be replaced periodically, because of the gradual buildup of a waxy deposit from the breakdown of the flexible tubing within the peristaltic pump, the introduction of nickel ions into the fresh distilled water should have maintained the longer lifetimes. There was possibly some extension of the foil lifetimes, but the statistics were too poor and there were too many other variables to be sure.

In spite of all our efforts, the average foil lifetime was never improved beyond about eight hours (although a few "Methuselahs" did mysteriously last as long as thirty hours). In any case, a safety system was needed to protect the accelerator vacuum system from the ingress of water following the catastrophic demise of a foil (pinhole leaks were quite rare). The cold trap shown in Figure 2 was the first line of defense. When the initial shock front struck the trap and attempted to penetrate the tube leading through it, most of the water would freeze on the trap. The water which missed capture by the trap caused a sudden rise in the pressure seen by the ion gauge located just upstream of the beam-defining aperture and, when the pressure rose above about 8×10^{-5} torr, a relay energized the solenoid of the fast-acting valve, located upstream of the ion gauge and beam defining aperture. As a backup, a second fast-acting valve, placed upstream of the first, was triggered by the ion gauge located above the final diffusion pump. Besides closing the vacuum valves, the relays also turned off the water pump, closed the solenoid valves on the entrance and exit water lines to the target cell, and triggered a loud alarm in the accelerator control room. With this system functioning properly, the accelerating tube pressure of the Van de Graaff accelerator was unaffected by a foil break.

If the electron spins are alternately directed parallel (+) and antiparallel (-) to the incident gamma ray momentum, corresponding to $\vec{S}_e \cdot \vec{p}_\gamma = \pm |\vec{S}_e||\vec{p}_\gamma|$, the following quantity can be constructed

$$\frac{N_+ - N_-}{N_+ + N_-} = \frac{\exp(-S_e p_\gamma \sigma_c \rho_e L) - \exp(+S_e p_\gamma \sigma_c \rho_e L)}{\exp(-S_e p_\gamma \sigma_c \rho_e L) + \exp(+S_e p_\gamma \sigma_c \rho_e L)})$$

$$\simeq - S_e p_\gamma \sigma_c \rho_e L \quad .$$

If we now define the analyzing power as $\eta = -S_e \sigma_c \rho_e L$,

$$\frac{N_+ - N_-}{N_+ + N_-} = \eta \, p_\gamma \quad ,$$

and we thus have a way to measure the circular polarization of a gamma ray, provided we know η. The determination of a value for the analyzing power will be deferred until Chapter V, Section A, where the experimental measurement of this quantity is discussed.

Two pairs of circular polarimeters, based on the theory above, were constructed for use in this experiment. The two sets were of the same basic design, but the second pair embodied certain improvements, most notably in the materials from which they were constructed. This second pair was used for 90% of the experiment and so will be discussed in detail below.

As shown in Figure 4, the polarimeters consist of an inner core and an outer casing to carry the flux from one end of the core back to the other end. The inner core was constructed from a 35% cobalt, 65% iron alloy, which has one of the highest known saturation magnetizations. The core is in the form of a spool, the ends extending to a larger radius so that the flux density will have decreased before the less permeable Armco

magnet iron, from which the magnetic return casing was constructed, begins to carry the flux. The return itself was constructed in two pieces, one shaped like a cup and the other like a circular plate, to allow assembly; there are channels through the joint between them for the electrical connections.

The polarimeters were powered by coils consisting of 520 turns of #18 gauge copper wire arranged in ten layers and encased in epoxy. They were placed at as large a radius as possible so that this lower Z, lower density material would not provide a low-attenuation multiple-bounce path to the detector. In addition to the power wiring, 3 turns of #30 gauge copper wire were wrapped directly around the core, approximately 2 cm from one end. These loops served as sense coils, in which an EMF was induced when the magnetic field in the core was changed. Integration of the signal from the sense coils provided a measurement of the magnetic flux in the core.

Between the core and the windings there was a thick cylindrical shell made from a machinable tungsten alloy which has a higher density than lead ($\rho \simeq 16$ grams cm^{-3}), and a rather high average Z. This shell served as shielding to absorb scattered gamma rays before they could enter the lower attenuation material in the coils; it was split into two pieces, separated by 1 mil of Mylar, in order to reduce the eddy currents produced when the direction of the magnetic field was switched. A combination lead and tungsten snout between the polarimeter and the target, and a lead collimator following the polarimeter prevented gamma rays not originally in the solid angle subtended by the detector from scattering from the outer portions of the polarimeter into the detector. A lead collar around the detector itself helped screen out gamma rays coming from any direction but that of the target.

Additional protection for the detectors was provided by placing lead bricks and boron-loaded paraffin bricks upstream of the counters, to shield them from gamma rays and neutrons created at the beam collimators. All of this shielding was required by the fact that only the unscattered gamma rays arising in the target and passing through the entire core of the polarimeters were of interest. Any other gamma rays simply contributed to the background, and to pulse pileup and deadtime problems.

The two identical polarimeters with their shields were positioned on opposite sides of the beam, at an angle of 100° to the beam direction. The polarimeters were powered in series along with a 0.2 ohm resistor by a steady state current of 4.75 amperes from a bipolar high-power operational amplifier. The sense of the electrical connections was such that the magnetic field was in the same direction for both polarimeter cores. However, since the polarimeters were located on opposite sides of the target, the dot product of the gamma ray momentum and electron spin was of opposite sign in the two polarimeters. A polarity switch allowed interchanging the leads to the polarimeters, so that the current flow and hence the field of the polarimeters could be reversed relative to the bipolar amplifier output.

Figure 5a illustrates the voltage signal which was supplied to the amplifier and to which the operational amplifier attempted to match the voltage drop across the 0.2 ohm sense resistor. The spike on the leading edge of each polarity change forced the amplifier to be momentarily overdriven to reduce the switching time as much as possible. Monitoring of the pickup coils around the cores of the magnets indicated that the magnet switching times were about 125 milliseconds. These coils also indicated that the steady state magnetic field in the cores was 23.7 kiloGauss.

One major source of changes in count rate which can mimic the effects of a circular polarization is the interaction of the beam with the stray, external magnetic field of the polarimeters. Measurements were therefore undertaken to determine the size of the horizontal component of the magnetic field along the path of the beam. Because the vertical field was so much weaker than the horizontal field (by a factor of at least ten), consistent measurements of the vertical field required greater precision in the positioning of the Hall probe than was practicable with the equipment available.

Figure 6a shows the results of measurements, along the beam path, of the change in horizontal magnetic field on reversing the polarimeter current (it is only the component of the stray field which changes polarity with the polarimeter current that is of interest here). Figure 6b shows these same results weighted by the distance from the target. The areas under the two curves are, respectively, -50.8 gauss-cm, indicating a vertical rotation of the beam direction by 2×10^{-4} radians, and -67.6 gauss-cm^2 indicating a vertical displacement of the beam by 2.7×10^{-4} cm. Assuming that the integrals of the vertical field are, like the field itself, a factor of ten or more smaller than the horizontal integrals, the implied horizontal rotation would produce an experimental asymmetry (the term will be defined in Chapter IV, which discusses the experimental results) of $\lesssim 6.4 \times 10^{-6}$ for a gamma ray with a relative a_2 angular distribution coefficient of 0.8. Again, assuming that the vertical integral is a factor of at least ten smaller, the horizontal beam displacement would create an asymmetry of $\lesssim 1.3 \times 10^{-6}$ in the entire detected pulse height spectrum. Such asymmetries are considerably smaller than the statistical accuracy achieved to date, 2×10^{-5}.

Still, the margin of safety can be improved by the addition of external, compensating fields to reduce the stray field of the polarimeters. This was accomplished by adding a set of coils around the outside of each polarimeter, and powering them in series with the polarimeters. Three different cancelling fields are shown in Figures 6c, e, and g; and their distance weighted values are shown in Figures 6d, f, and h. Figures 6c and d represent the effect of a compensation field, used for approximately 12% of our data, which was designed to reduce the displacement of the beam at the target as indicated by the factor of seven decrease in the area under the distance weighted curve. An effective horizontal displacement of the average target spot position can also be produced by a vertical beam displacement if a collimator partially occults an off-center beam. This problem is addressed by the fields in Figures 6e and f and Figures 6g and h, which are successive approximations to fields for which the upstream contribution has been reduced as much as possible; these compensation fields were used for 10% and 46% of the data, respectively.

There is still another mechanism by which the stray magnetic field of the polarimeters may create a false asymmetry. A state with a large g-factor and a long lifetime may precess through a significant angle in a magnetic field and thus have its decay angular distribution rotated. The ^{18}F state at 937 keV is fed from such a state, the 1122 keV state. Further discussion of this effect will be reserved for the section dealing with the experimental attack on this problem (Chapter V, Section B).

E. Detection, Sequencing and Data Accumulation

For detection of the gamma rays transmitted through the polarimeters, two nominally 75 cc, 15%, lithium-drifted germanium detectors (from Princeton

Gamma Tech) were available. For each Ge(Li) detector, the output from the preamplifier was fed into a Tennelec 205A linear amplifier. The count rate, which was maintained at about 30,000 counts/sec in each detector, was sufficiently high that the best pulse height resolution was attained with amplifier differentiation and integration time constants of only one microsecond, although longer time constants are more usual for Ge(Li) detector work. Active baseline restoration was used to return the trailing edge of the pulses to a zero DC level as quickly as possible.

The outputs of the amplifiers were DC-coupled to two Nuclear Data 100 MHz Analog-to-Digital Converters (ADC). The digital zero suppression and the analog gates of these ADC's were used to restrict pulse height digitizing to an energy window of approximately 400 keV. This window was positioned to record not only the peak from the 1081 keV gamma rays of principal interest, but also from gamma rays at energies of 937, 1020, 1042, and 1164 keV, as seen in the sample spectrum of Figure 7. Reference to Figure 1 reveals that the 937, 1042, and 1081 keV peaks all arise from transitions to the ground state from states with those excitation energies, but that the 1020 and 1164 peaks stem from the decay of the 2101 keV state to the 1081 and 937 keV states, respectively. The necessity of cleanly separating the 1020 and 1042 keV gamma ray peaks sets the stringent requirements for energy resolution in the present experiment.

Besides the Ge(Li) pulses, the ADC's also received an input from the time sequencer which controlled the experiment. The signals from this unit are displayed in Figure 5a, and its interconnections with the rest of the electronics are depicted in Figure 5b. In addition to supplying the

driving signal for the polarimeter power supply as mentioned earlier, the sequencer generated a signal which blocked the ADC's from analyzing pulses arriving during an interval of 130 milliseconds starting 1 millisecond before the magnet switching began (the length of this blocking interval was set digitally, and other blocking lengths were also used at various times). A third signal, with the same 4 second period as the polarimeters, was used to route the pulses occurring during either of the two magnet polarities into the appropriate sections of memory in the multichannel analyzers. Again, as for the polarimeter current signal, switching from one state of routing to the other occurred 1 millisecond after the ADC's had been blocked, so that there was no possibility of confusion within the analyzers as to where pulses should be stored. Finally, a single pulse was generated for every complete four-second cycle, which was fed into a scaler and used to keep track of the number of cycles. The four-second cycle period was digitally controlled and was used for almost all of the data taking.

The digital outputs of the two ADC's were fed into one of two alternate storage systems. For the first 30% of the experiment a single, computer-based Nuclear Data 4420 system received the inputs from both ADC's. This system had several disadvantageous features from the point of view of the present experiment, although none of these was shown to lead to detectable false effects: 1) Because the system could service only one ADC at a time, the dead time seen by one counter would vary with the count rate in the other, 2) the two ADC's were not granted equal probability of being serviced, one having slightly higher priority than the other, and 3) the system generated a dead time, which was not related

to the input pulses, in order to update a visual display of memory. Thus, during the remainder of the experiment, separate Nuclear Data 2400 Multichannel Analyzers were provided for each of the two Ge(Li)'s. Because the two analyzers were independent, their dead times were uncorrelated; and each ADC naturally had complete service priority by its own analyzer. Finally, the design of these analyzers was such that at the high experimental count rate, they suspended their normal display cycle and, instead, briefly illuminated the channel being serviced. The high experimental count rate produced a nearly continuous display, which was quite adequate to monitor the data acquisition visually.

The deadtime of the analyzers is a matter of some concern because of the tendency of dead time effects to smooth count rate fluctuations. The dead time loss of counts reduces the fraction of counts recorded when the count rate goes up, and increases the fraction of counts recorded when the count rate goes down. The dead time meters on the ADC's typically indicated a dead time of about 20% during the data acquisition. Although these meters average the dead time over a period of about 100 milliseconds, the beam intensity was sufficiently steady that the instantaneous dead time was probably within 20% of that number.

An even more insidious effect is caused by pulse pileup, which again acts to smooth out count rate variations, but this time does so especially for the spectrum peaks. If the count rate goes up for the entire spectrum, the increase in the number of counts recorded in a peak will be reduced by the increased pulse pileup moving more counts out of the peak than are moved into it from surrounding background regions by pileup. Thus, the sum of dead time and pileup effects together was such that only about half of the full energy pulses produced by the incident gamma rays were stored in

the appropriate channels of the analyzers. By the same reasoning, increasing the input pulse rate to the analyzers rapidly produced increased losses from the peaks as well as poorer pulse height resolution.

Data accumulation in the analyzers was stopped briefly every 2000 cycles, corresponding to approximately two hours. The four accumulated spectra resulting from the two field directions, in the two counters, were written on magnetic tape three times, the analyzers were cleared, and the process of acquiring spectra was then begun again, all under automatic control. The magnetic tapes were read into an off-line computer, where the three copies of each data dump were checked against one another for possible tape errors. Master tapes were then prepared in a form which could be more easily read by the off-line computer.

The computer processed the master tapes dump by dump, by first locating the five gamma-ray peaks in each spectrum. It then defined regions about these peaks ten channels wide (other widths were also tried but ten channels seemed to be the best compromise), where the center of each peak region was picked by a parabolic fit to the top three points in the peak. Five background regions, one between each pair of adjacent peaks, except between the 1020 and 1042 keV peaks, as well as one region below the lowest peak and one above the highest, were also defined. The number of counts in each region was summed, partial channels being fitted by a quadratic interpolation formula, and the asymmetry, a quantity to be defined in the next section, was calculated. Figure 7 shows the ten regions, 5 peaks, and 5 backgrounds in a typical spectrum.

IV. EXPERIMENTAL RESULTS

The physical details of how the experiment was carried out have been discussed in Chapter III. Now we turn to the question of how to display and interpret the data which were collected by that procedure. The first step in answering that question is to understand the meaning and significance of a quantity alluded to earlier, the asymmetry.

A. Asymmetry

In Chapter III we discussed the measurement of a quantity which was the product of the circular polarization of a gamma ray, P_γ, and the polarimeter analyzing power, η, for a single polarimeter. Now we must consider how best to combine the effects from two polarimeters. Let the symbol "+" label the half of the data-taking cycle when the electron spins in the polarimeter on the right of the beam (looking downstream) point away from the target. From the earlier derivation we know that

$$P_\gamma \eta_R = \frac{R_+ - R_-}{R_+ + R_-} \quad \text{and} \quad P_\gamma \eta_L = \frac{L_- - L_+}{L_+ + L_-}$$

where $R_\pm (L_\pm)$ designates the number of counts recorded on the beam right (left) during the subscripted half cycle. The sign of the expression for the left polarimeter is opposite to that for the right polarimeter because the dot product of the electron spin and the gamma ray momentum has opposite sign in the two polarimeters [see page 22]. Averaging the two expressions and assuming $\eta_R = \eta_L$ yields

$$P_\gamma \eta = \frac{1}{2}\frac{R_+ - R_-}{R_+ + R_-} + \frac{1}{2}\frac{L_- - L_+}{L_+ + L_-}$$

$$= \frac{1}{4}\left(1 - \frac{R_-}{R_+}\right) + \frac{1}{4}\left(1 - \frac{L_+}{L_-}\right) + O(\varepsilon^2)$$

$$= \frac{1}{4}\left(1 - \frac{L_+R_-}{L_-R_+} + \frac{L_+R_-}{L_-R_+} + 1 - \frac{R_-}{R_+} - \frac{L_+}{L_-}\right) + O(\varepsilon^2)$$

$$= \frac{1}{4}\left(1 - \frac{L_+R_-}{L_-R_+}\right) + \frac{1}{4}\left(1 - \frac{R_-}{R_+}\right)\left(1 - \frac{L_+}{L_-}\right) + O(\varepsilon^2)$$

$$= \frac{1}{4}\left(1 - \frac{L_+R_-}{L_-R_+}\right) + O(\varepsilon^2)$$

$$\simeq \frac{1}{4}\left(1 - \frac{L_+R_-}{L_-R_+}\right) \quad ,$$

where ε is the fractional change in count rate between the two senses of the polarimeter magnetization which is small compared to unity. Terms proportional to epsilon squared or higher powers have been grouped in the symbol $O(\varepsilon^2)$ and then dropped.

We define the right hand side of the expression above to be the asymmetry, A. This form clearly illustrates the insusceptibility of the measurements to certain types of error. For instance, if the number of ^{18}F nuclei created during one route (one half-cycle) does not equal the number during the other (due to beam intensity fluctuation, timing error, etc.), one counter alone would see a change in count rate which might be interpreted as a circular polarization. However, the second counter would see a similar variation in count rate but interpret it as a circular polarization of opposite sign. By combining the two in the asymmetry as defined, the false apparent polarizations automatically cancel each other.

Unfortunately, there are other sources of count rate variations which may lead to asymmetries that do not cancel. Some, such as horizontal movement of the beam spot in synchronism with the change in routing signal, will not be energy (pulse height) dependent (or only weakly so). Thus, if one looks at the asymmetry of adjacent regions in the pulse height spectrum, one can correct for such effects. Others are solely properties of parts of the data collecting system; thus, if the current leads to the two polarimeters are interchanged, the sign of the asymmetry arising from a genuine circular polarization would remain unchanged (because the + route was defined in terms of the electron spin direction within the right counter), while the sign of an asymmetry caused by some failure in the electronic circuits would change because the fault would then occur in what is defined to be the opposite half of the routing cycle. By combining equal amounts of data taken for the two directions of polarimeter lead hookup, the false asymmetry will be canceled.

Finally, there are some effects which operate only in specific regions of the pulse height spectrum. Rotation of the beam direction in the horizontal plane (by stray magnetic fields) in synchronism with the change in routing signal will affect only those regions of the spectrum which arise from radiation with a strongly anisotropic angular distribution. Similarly, the precession of an excited state in the component of the stray vertical magnetic field which switches with the polarimeters can lead to asymmetries in subsequent gamma rays if the state's g-factor, lifetime, and anisotropy are large. In general, it is obvious that stray magnetic fields should be kept as small as possible. Beyond this, one must determine those regions which are susceptible to such effects,

estimate the size of the asymmetries produced, and then, if the false asymmetries may be significant, eliminate these regions from consideration.

Besides all of these "false" asymmetries, there may be regions of the pulse height spectrum which exhibit an asymmetry arising from a true circular polarization. The propensity of the ^{3}He beam to create positron emitters (including the nucleus of interest) means that bremsstrahlung and annihilation-in-flight gamma rays from the resulting positrons will be partially righthand circularly polarized. Fortunately, this polarization should vary smoothly with photon energy so that the asymmetry to be expected in some chosen region of the pulse height spectrum may be found by extrapolation from adjacent regions.

Of course, any of the sources of spurious asymmetry may be functions of the setup parameters, modifications to the equipment, and other parameters which vary between data-taking sessions. A chronological breakdown of the data may, therefore, help to reveal the presence of such a false asymmetry.

B. Data

Pulse height spectra for ^{18}F gamma rays were accumulated during fifteen data-taking sessions between September 1975 and August 1977 for a total of approximately 1500 hours. Figures 8a and b show the asymmetries of the five peak regions and the five background regions, respectively, observed in each data-taking session, while the polarimeter power leads were hooked up in a manner we will label "normal". The leads were attached to the power supply in the "reverse" order when the asymmetries in Figures 8c and d were recorded. A chronology of the sessions and of any

modifications to the experiment is given in Table I. There are no strong, systematic variations apparent in any of the regions or between one region and another.

The total asymmetries for the "normal" points, for the "reverse" points and for the sum of the two are shown in Figure 9a as functions of their positions in the pulse height spectrum. The reduced chi-squares about those totals are graphed in Figure 9b, again versus energy. All of these results are summarized in Table II. There does appear to be a slight positive offset in the "reverse" runs. In the next section we will discuss how the effect of such offsets, as well as the diluting, and possibly distorting, effect of the background under the peaks can be removed.

C. Extraction of Peak Asymmetry

The asymmetry of a peak region includes not only the contribution from the peak itself, but also a contribution from the continuous background underneath that peak. To remove the effect of this background consider the asymmetry, A, in terms of the counts seen in the left, L, and right, R, counters during either the plus (+) or minus (-) route. By superscript, we will denote whether these counts are in the peak (P), the background (B), or the total (T). By definition,

$$A^P = \frac{1}{4}\left(1 - \frac{L_+^P}{L_-^P}\frac{R_-^P}{R_+^P}\right) \quad ,$$

from which one obtains

$$1 - 4A^P = \frac{L_+^P R_-^P}{L_-^P R_+^P} = \frac{(L_+^T - L_+^B)}{(L_-^T - L_-^B)}\frac{(R_-^T - R_-^B)}{(R_+^T - R_+^B)}$$

$$= \frac{1}{(1-f_L)}\frac{1}{(1-f_R)}\frac{(L_+^T - L_+^B)}{L_-^T}\frac{(R_-^T - R_-^B)}{R_+^T} \quad ,$$

where $f_{L(R)}$ denotes the fraction of the total counts which are from the background in the left (right) detector during the minus (plus) route. For convenience, define: $F = (1 - f_L)(1 - f_R)$. Then, multiplying out the step above yields:

$$1 - 4A^P = \frac{1}{F}\left[\frac{L_+^T}{L_-^T}\frac{R_-^T}{R_+^T} + \frac{L_+^B}{L_-^T}\frac{R_-^B}{R_+^T} - \frac{L_+^B}{L_-^T}\frac{R_-^T}{R_+^T} - \frac{L_+^T}{L_-^T}\frac{R_-^B}{R_+^T}\right]$$

$$= \frac{1}{F}\left[(1 - 4A^T) + f_L f_R(1 - 4A^B) - f_L\frac{L_+^B}{L_-^B}\frac{R_-^T}{R_+^T} - f_R\frac{L_+^T}{L_-^T}\frac{R_-^B}{R_+^B}\right] \quad .$$

Examine the third term more carefully:

$$f_L\frac{L_+^B}{L_-^B}\frac{R_-^T}{R_+^T} = f_L\sqrt{\frac{L_+^B}{L_-^B}\frac{R_-^B}{R_+^B}\;\frac{R_+^B}{R_-^B}\frac{L_+^B}{L_-^B}\;\frac{R_-^T}{R_+^T}\frac{L_-^T}{L_+^T}\;\frac{L_+^T}{L_-^T}\frac{R_-^T}{R_+^T}}$$

$$= f_L\sqrt{(1 - 4A^B)}\;\sqrt{\frac{R_+^B}{R_-^B}\frac{L_+^B}{L_-^B}\Big/\frac{R_+^T}{R_-^T}\frac{L_+^T}{L_-^T}}\;\sqrt{(1 - 4A^T)}$$

A^B and A^T are both $<<1$. The ratio in the middle of the expression above looks at the fractional difference in the counts for the two routes as seen in the background and in the total. This ratio should differ from unity at most by some small amount, ε; in which case

$$f_L\frac{L_+^B}{L_-^B}\frac{R_-^T}{R_+^T} \simeq f_L(1 - 2A^B)(1 + \tfrac{1}{2}\varepsilon)(1 - 2A^T) \quad .$$

Using the same line of reasoning, the fourth term in the expression for A^P becomes

$$f_R\frac{L_+^T}{L_-^T}\frac{R_-^B}{R_+^B} \simeq f_R(1 - 2A^B)(1 - \tfrac{1}{2}\varepsilon)(1 - 2A^T) \quad .$$

Summing these two terms leads to

$$f_L \frac{L_+^B}{L_-^B}\frac{R_-^T}{R_+^T} + f_R \frac{L_+^T}{L_-^T}\frac{R_-^B}{R_+^B} = (f_L + f_R)(1-2A^B)(1-2A^T)$$

$$+ (f_L - f_R)(1-2A^B)(1/2\ \varepsilon)(1-2A^T) \quad .$$

Because of the similarity of the two counters used in this experiment, f_L and f_R are the same within about 5 percent, so that the second term above is at most second order in small quantities, and is small in comparison with the first order pieces of the first term; it therefore can be dropped.

Substituting this value into our expression for A^P yields

$$1-4A^P = \frac{1}{F}\left[(1-4A^T) + f_L f_R(1-4A^B) - (f_L + f_R)(1-2A^B)(1-2A^T)\right] .$$

Solving this expression for A^P and discarding terms of second order in small quantities gives

$$A^P = \frac{1-\frac{1}{2}f_L - \frac{1}{2}f_R}{(1-f_L)(1-f_R)} A^T - \frac{\frac{1}{2}f_L + \frac{1}{2}f_R - f_L f_R}{(1-f_L)(1-f_R)} A^B \quad .$$

If we now define $f = \dfrac{1/2\ f_L + \frac{1}{2}f_R - f_L f_R}{1 - \frac{1}{2}f_L - \frac{1}{2}f_R}$ (Note: if $f_L = f_R$ then $f = f_L = f_R$) this equation assumes the simple form

$$(1-f)A^P = A^T - fA^B \quad ,$$

which could easily have been arrived at on intuitive grounds.

As a result of some subtle failure of the measurement system, an additional asymmetry may appear in the spectrum, even in those areas

which theoretically should have no asymmetry; this additional asymmetry will be called a null shift asymmetry. By returning to the definition of the asymmetry, we can easily derive an expression to remove the effect of a null shift, A^N, from an observed asymmetry, A^O, to obtain the true asymmetry, A. A null shift results when one or more of the count totals which enter the asymmetry ratio is modified away from the value it would have had in the absence of the null shift. Thus, using epsilon to represent the fractional deviation, we have

$$A^O = \frac{1}{4}\left(1 - \frac{L_+^O R_-^O}{L_-^O R_+^O}\right)$$

$$1 - 4A^O = \frac{L_+(1+\varepsilon_1)}{L_-(1+\varepsilon_2)} \frac{R_-(1+\varepsilon_3)}{R_+(1+\varepsilon_4)}$$

$$\simeq (1-4A)(1+\varepsilon_1 - \varepsilon_2 + \varepsilon_3 - \varepsilon_4) \quad .$$

If we now identify $-\varepsilon_1 + \varepsilon_2 - \varepsilon_3 + \varepsilon_4 = 4A^N$, we find

$$1 - 4A^O = -4A - 4A^N + 1 \quad ,$$

and

$$A = A^O - A^N \quad ,$$

where second order terms have been dropped. (Note: A = 0 implies $A^O = A^N$).

The equations for the removal of background and null asymmetries can be applied to the asymmetries of the peak regions of the ^{18}F spectrum if values can be determined for the background and the null shift asymmetries in the neighborhood of the peaks. A background value can be obtained for any spectral region if the five measured background

region asymmetries are used to determine an interpolation formula. Zeroth, first and second degree polynomials in the energy were fitted to the five background values by a least-squares fitting procedure (see Table III). By using the expression given above for removing a background asymmetry, the peak asymmetries listed in Table IV are obtained.

At this point in the analysis, the obvious next step would be to remove from the asymmetry of the 1.08 MeV peak the effect of any null asymmetry. Such a null shift can in principle be determined from the observed peak asymmetries of the 1.02, 1.04, and 1.16 MeV gamma rays if the true value of these peak asymmetries is assumed to be zero (the 0.937 peak is excluded because of its susceptibility to a fake asymmetry as discussed in Chapter V, Section B). Based on constant and linear-polynomial least-square fits to the three sets of peak asymmetries, null shifts have been subtracted from the appropriate values of the 1.08 MeV asymmetry; the results have been listed in Table V.

However, this procedure fails to take into account the knowledge about possible offsets obtained from the tests carried out in complementary experiments with pulsers, ^{60}Co sources and enhanced magnetic fields (see Chapter V), all of which imply the absence of any null or instrumental asymmetry. The presence of a null asymmetry in the analyzing power determination (Chapter V, Section A) is completely consistent with an explanation in terms of a deadtime-pileup asymmetry induced by the asymmetry in the total count rate. Such a mechanism will not introduce a large asymmetry in the case of the ^{18}F spectra because the total count rate asymmetry is so small [even if the total spectrum asymmetry is the same as the average observed asymmetry of

$(0.6 \pm 0.7) \times 10^{-5}$ (excluding the 0.937 MeV peak) the observed peak losses of $\sim$50 percent imply a null asymmetry of only $(-0.6 \pm 0.7) \times 10^{-5}$]. In light of this argument, a typical value of $A^N = (-2.4 \pm 3.1) \times 10^{-5}$ as shown in Table V appears unrealistically large.

An alternative to removing the measured values of A^N, which would clearly increase the statistical uncertainty, is to assume that the null asymmetry is identically zero. This means the observed peak asymmetries listed in Table IV are also the true peak asymmetries. Assuming that A^N is zero is entirely consistent with the 1.02, 1.04, and 1.16 MeV peaks having no true asymmetry; the linear-background values, for example, have a reduced chi-square of 1.18 about zero, which corresponds to a 30% probability of getting an equal or larger reduced χ^2 by chance.

A second alternative is to assume that there is no background asymmetry, only a null shift. Thus it could be argued that the observed asymmetries are caused by such mechanisms as beam displacements and/or systematic count rate variations. This assumption would be clearly invalid if the background possesses some asymmetry which would not appear in the peaks, such as the presence of a true circular polarization from the annihilation-in-flight of high energy beta rays. Table VI contains the numerical results for the null shift at the energy of the 1.08 MeV peak determined from fits to the five background regions and three of the four (excluding the 0.937 MeV peak) remaining peak regions. These null shifts have been removed and the peak asymmetries then corrected for the diluting effect of background included in the region, to yield the results shown in the final column of Table VI.

$(0.6 \pm 0.7) \times 10^{-5}$ (excluding the 0.937 MeV peak) the observed peak losses of $\sim$50 percent imply a null asymmetry of only $(-0.6 \pm 0.7) \times 10^{-5}$]. In light of this argument, a typical value of $A^N = (-2.4 \pm 3.1) \times 10^{-5}$ as shown in Table V appears unrealistically large.

An alternative to removing the measured values of A^N, which would clearly increase the statistical uncertainty, is to assume that the null asymmetry is identically zero. This means the observed peak asymmetries listed in Table IV are also the true peak asymmetries. Assuming that A^N is zero is entirely consistent with the 1.02, 1.04, and 1.16 MeV peaks having no true asymmetry; the linear-background values, for example, have a reduced chi-square of 1.18 about zero, which corresponds to a 30% probability of getting an equal or larger reduced χ^2 by chance.

A second alternative is to assume that there is no background asymmetry, only a null shift. Thus it could be argued that the observed asymmetries are caused by such mechanisms as beam displacements and/or systematic count rate variations. This assumption would be clearly invalid if the background possesses some asymmetry which would not appear in the peaks, such as the presence of a true circular polarization from the annihilation-in-flight of high energy beta rays. Table VI contains the numerical results for the null shift at the energy of the 1.08 MeV peak determined from fits to the five background regions and three of the four (excluding the 0.937 MeV peak) remaining peak regions. These null shifts have been removed and the peak asymmetries then corrected for the diluting effect of background included in the region, to yield the results shown in the final column of Table VI.

D. The Circular Polarization of the 1.081 MeV Gamma Ray

We now have twelve different answers to the question of the asymmetry of the 1.081 peak: 6 from the 3 background fits with either of the 2 null fits; 3 from the 3 background fits, assuming that the null shifts are zero, and 3 from the 3 null fits, assuming that the true background asymmetries are zero. Fortunately, the differences among the various answers are not statistically significant. However, rather than continuing with all twelve values, we adopt the values from those fits with the lowest reduced chi-square as being typical, thus giving the three values listed in Table VII, which correspond respectively to the linear background-constant null fit, the linear background-zero null fit, and the linear null-zero background fit. In Chapter V, Section A, we have obtained a value of $(+1.88 \pm 0.05) \times 10^{-2}$ for the analyzing power of the circular polarimeters. Dividing this value into the peak asymmetry values yields the values for the circular polarization given in the second column of Table VII.

E. Comparison with Theory

The stated goal of this experiment was to check a prediction of Gari et al. (1975) that the circular polarization of the 1.081 MeV gamma rays from the 0^-, T = 0 state in the nucleus ^{18}F was $P_\gamma = 5.7 \times 10^{-3}$. By referring to Table VII, we see that all three of the adopted experimental values are inconsistent with that value by at least two standard deviations. Taking the linear-background-no-null result as the most reasonable interpretation of the data, we find that the discrepancy is either 2.4 or 3.1 standard deviations (depending on the

sign assumed for the theoretical prediction and ignoring possible uncertainties in the prediction), corresponding to 0.85% chance of agreement.

During the time the experiment was in progress, the enhancement prediction of Gari and Reid (1974) was superseded by new estimates of the enhancement to be expected in the Weinberg-Salam model. If the experimental polarizations in Table VII are divided by the charged-current prediction of Gari et al., the limits on the enhancement factor given in Table VII are obtained. These values can be compared with an enhancement factor of 8 to 10 predicted by Desplanques and Micheli (1977). The difference between their predicted enhancement and the observed values is approximately one standard deviation (1.2 or 1.9 sigma, using the linear-background-no-null value, corresponding to a 15% probability of agreement). Such a discrepancy cannot be considered very significant. Because this enhancement factor was calculated with a value of $\sin^2\theta_W = 0.36$, a value which now appears too large (Abbott and Barnett 1978), a 10% decrease in the predicted enhancement should be applied, further reducing the discrepancy.

Besides the Weinberg-Salam model, various other models have been proposed to deal with the problems of the Cabibbo model. Unfortunately, no detailed calculation of the effects of these models on the isovector, parity-violating weak nuclear potential has been carried out. The exceptions to this statement are those theories which, by construction, have no parity violation in the non-Cabibbo portions of the Hamiltonian (see Hung and Sakurai 1977, Galić and Tadić 1976, and references cited therein). The results to date of the present experiment are clearly

consistent with the models predicting no enhancement.

A final prediction arises from an empirical fit by Box et al. (1976) to the results of other parity-violation experiments. Two possible enhancements of the conventional potential were obtained, 6.9 or 11.8, with a slight preference for the smaller value. This value is, again, not inconsistent with the results listed in Table VII.

Clearly, an effort to reduce the uncertainty on the present results is warranted. A factor of two decrease in the error would be reasonably certain to provide a meaningful test of the current predictions; however, because the error is purely statistical in nature, at least at the present level, a factor of four increase in the total number of counts is required to achieve a factor of two decrease in the uncertainty. With a somewhat optimistic duty factor of 25%, this would require a two year program with the existing experimental set-up. Doubling the number of polarimeter-detector combinations would reduce this time by a factor of two, as well as canceling some additional possible sources of false asymmetries. The expense of providing a duplicate of the current set-up may, however, be prohibitive. Alternatively, the more selective $^{21}Ne(p,\alpha)^{18}F$ reaction (Q = -1.74 MeV) might be tried. This reaction could avoid the excitation of the 2.1 MeV state and higher states of ^{18}F which would not only significantly reduce the background under the 1.08 gamma ray peak, but also eliminate the somewhat troublesome 1.02 and 1.16 MeV gamma rays. Unfortunately, serious problems of target development and cost would still remain. How ever further measurements are carried out, the ^{18}F nucleus remains one of the most favorable cases, both experimentally and theoretically, for

studying the isovector, parity-nonconserving, nucleon-nucleon force.

In summary, a value for the circular polarization of the 1081 keV gamma ray from ^{18}F has been obtained which is consistent with zero, and smaller than but not inconsistent with the most recent predictions based on the Weinberg-Salam theory of neutral currents. A list of parity violation experiments involving the nucleonic weak current has been provided in the Supplementary Table. Many of the entries in the table indicate parity-violating effects differing by more than one standard deviation from zero. Unfortunately, the present experimental and theoretical uncertainties preclude drawing any firm conclusions about the nature of the nucleonic neutral weak current.

V. SUBSIDIARY MEASUREMENTS

In order to interpret the results from the ^{18}F asymmetry measurement, certain subsidiary measurements were necessary. The most important of these was the determination of the analyzing power of the circular polarimeters.

A. Analyzing Power Measurement

As we showed in Chapter II, Section D, the result of passing a gamma ray beam through a circular polarimeter is to measure the product $A = P_\gamma \eta$ where P_γ is the circular polarization of the gamma rays and η is the analyzing power of the polarimeter. In order to determine the polarization, the analyzing power must be known. Since we have already shown that $\eta = -S_e \rho_e \sigma_c L$, one approach to obtaining a value for η is to calculate it from the various quantities in this expression.

A.1 Calculated Value

The product $S_e \rho_e$ can be determined from a measurement of the magnetic induction, B (MKS units will be used throughout this discussion). The magnetization, M, within the core of the polarimeter is given by $M = \mu_B S_e \rho_e$ and $B = \mu_o(M+H)$, where μ_B is the Bohr magneton $= \frac{e\hbar}{2m_e}$, μ_o is the permeability of free space $= 4\pi \times 10^{-7}$ (kg m /coul^2), and H is the magnetic field intensity. The magnetic induction, B, was measured by "integrating" the EMF induced in the pickup coils around the polarimeter cores, when the field was switched from one direction to the other. (The integration network consisted of a capacitor charged through a resistor.) This procedure for determining B was calibrated by quickly removing a similar pickup coil from the NMR-measured field of the 90° energy-

analyzing magnet of the ONR-CIT tandem accelerator. The voltage signal observed on the capacitor at an excitation current of 4.5 amperes implied $B = 2.371 \pm 0.074$ tesla in the cores of the polarimeters. If H is assumed to be that for a long solenoid (NI ampere turns per meter), $\mu_o H = 0.048$ tesla (tesla = kg / coul-sec). Eliminating the magnetization M from the two equations given above yields

$$S_e \rho_e = \frac{(B - \mu_o H)}{\mu_o \mu_{Bohr}}$$

$$= (2.00 \pm 0.06) \times 10^{29} \text{ polarized electrons/m}^3 .$$

If the density of the 35% Co-65% Fe polarimeter is taken to be 8.25 g/cc, this value implies an average of 2.29 polarized electrons per atom.

The polarization-dependent portion of the Compton cross section is given by the expression (see Chesler 1965 and references cited therein)

$$\frac{\sigma_c}{2\pi r_o^2} = \frac{1 + 4E + 5E^2}{E(1+2E)^2} - \frac{(1+E)\ \ell n(1+2E)}{2E^2}$$

where r_o is the classical electron radius ($= 2.818 \times 10^{-15}$ meters) and E is the energy of the gamma ray in units of the electron mass. For the 1.081 MeV gamma ray, $\sigma_c = -1.293 \times 10^{-30}$ m^2.

The length L of magnetized material traversed by the gamma rays is more difficult to calculate precisely because, up to now, the effect of the end plates of the polarimeters has been ignored. There the field must turn outward to enter the outer return casing, and may vary in both direction and magnitude from point to point. If the

permeability of the alloy is assumed to be constant, the component of $\vec{S}_e$ along the gamma ray momentum will vary linearly with the component of $\vec{B}$ along the axis. The effective length of the end plates then can be obtained by comparing the average field parallel to the axis in the end cap with the average field in the core.

An approximation for the ratio of the end plate axial field component to the core field can be obtained by considering the problem of the field within a cylinder of radius a and height b (where a is the radius of the core and b is the thickness of the end plate). Within this cylinder $\vec{\nabla} \times \vec{H} = 0$ and $\vec{\nabla} \cdot \vec{B} = 0$. Therefore, assuming μ is constant, $\vec{B}$ may be chosen to be the gradient of ψ, where ψ is a scalar potential satisfying Laplace's equation $\nabla^2\psi = 0$. Furthermore, $B_z = \frac{\partial \psi}{\partial z}$ and $\nabla^2\psi = 0$ implies $\nabla^2 B_z = \nabla^2(\frac{\partial \psi}{\partial z}) = \frac{\partial}{\partial z}(\nabla^2\psi) = 0$. Thus the component of B parallel to the cylindrical axis satisfies Laplace's equation also.

We can solve for B_z with the following boundary conditions: 1) B_z on the top surface = 0, 2) B_z on the cylindrical surface = 0, and 3) B_z on the bottom surface = B_o, where B_o is the field in the core. In this model the flux enters the cylinder through the bottom surface parallel to the cylinder axis and exits perpendicularly through the cylindrical sides with no flux leaking out of the top surface. The solution is

$$B_z = \sum_n \frac{2B_o}{\alpha_n} \frac{\sinh[\frac{\alpha_n}{a}(b-z)]}{\sinh[\frac{\alpha_n}{a} b]} \frac{J_0(\frac{\alpha_n}{a}\rho)}{J_1(\alpha_n)} \quad ,$$

where J_N is the N^{th} Bessel function, α_n is the n^{th} zero of J_0, and z and ρ are the ordinary cylindrical coordinates with origin at the center

of the bottom surface.

Averaging this expression over the volume of the cylinder yields

$$\frac{\overline{B}_z}{B_o} = \sum_n 4 \frac{a}{b} \frac{\cosh(\alpha_n \frac{b}{a}) - 1}{\alpha_n^3 \sinh(\alpha_n \frac{b}{a})} \quad .$$

The polarimeter design used in this experiment has $\frac{a}{b} = 1.818$, so $\overline{B}_z/B_o = 0.36$.

Assignment of an uncertainty to this calculated value of the effectiveness of the end cap length is difficult, but a conservative estimate might be $B_z/B_o = 0.36 \pm 0.10$.

If we combine all these pieces of the analyzing power, we obtain

$$\eta_{cal} = (1.824 \pm 0.075) \times 10^{-2} \quad .$$

A.2 Theory of the Measurement

An alternate method for determining the analyzing power of the circular polarimeters is by measurement. If one considers the attenuation of an unpolarized beam of gamma rays in a magnetized medium, the original incident intensity, I_o, of the beam can be decomposed into two equal parts, one right-circularly polarized, I_{o+}, and one left, I_{o-}. Following the notation of Chapter III, Section D, the intensity after passing through a length, L, of material with S_e along the direction of the gamma-ray propagation will be

$$I_{\pm} = \frac{1}{2} I_o \exp[-(\sigma_o \pm S_e \sigma_c)\rho_e L] \quad .$$

The polarization of the transmitted beam is then

$$P_\gamma = \frac{I_+ - I_-}{I_+ + I_-} \simeq -S_e \rho_e \sigma_c L \quad .$$

This is precisely the definition of the analyzing power η. Thus, if a second equal length of magnetized medium is used to analyze the gamma ray beam that is transmitted through the first length, an asymmetry equal to the square of the analyzing power will be observed.

A.3 Experimental Procedure

A beam of unpolarized gamma rays was provided by a 1.26 Curie ^{60}Co source encased in a 25 cm diameter sphere of uranium depleted in ^{235}U. A 1.27 cm diameter lead collimator allowed a narrow beam of 1173.2 keV and 1332.5 keV gamma rays to escape.

The two polarimeters described earlier were arranged one after the other in the gamma ray beam (see Figure 10). The polarimeter closest to the source was powered by a static power supply and served as a polarizer. The bipolar power amplifier system used in the ^{18}F portion of the experiment provided the current for the second polarimeter, which served as analyzer. Lead collimators were again used to reduce the flux of scattered gamma rays by-passing the cores of the two polarimeters.

Except for two modifications, the detection, sequencing, and data accumulation system was the same as in the principal part of the experiment. Since only one Ge(Li) detector was used, both amplifier-ADC-multichannel-analyzer systems received the output of the same detector and preamplifier. Secondly, the preamplifier test input was fed by a Berkeley Nucleonics Corporation random pulse generator, Model DB-2. The amplitude of the pulses from this generator was adjusted to

correspond to a gamma ray peak of either 1036 keV or 1456 keV; these values were chosen to give peaks either below or above the two ^{60}Co peaks.

Although the total counting rate was only 20,000 counts/second (much lower than the 25,000 to 35,000 counts per second in the ^{18}F experiment) approximately 34 percent of the input counts from the pulser failed to appear in that peak in the recorded spectrum. Also, in spite of the fact that the total count rate from the ^{60}Co source was lower than in the ^{18}F measurement, the much higher percentage of counts in the peaks required the analyzers to be dumped every 1000 cycles instead of the 2000 cycles employed in the ^{18}F data collection.

The computer analysis of the data was similar to that done in the ^{18}F portion of the experiment except that a modified definition of the asymmetry was required by the absence of a second detector. Besides the three peak regions, either five or six background regions were defined, and asymmetries were calculated for all these regions. The backgrounds corresponded to regions above and below each peak except that during the runs when the pulser was set to the higher energy value, the background regions above the 1332 keV peak and below the pulser were combined into a single region for statistical reasons.

A.4 Experimental Results

An asymmetry for this single-detector case can be defined in a fashion similar to the asymmetry defined earlier:

$$\eta^2 = \frac{N_+ - N_-}{N_+ + N_-}$$

$$= \frac{1}{2}\left(\frac{N_+}{N_-} - 1\right) \equiv A$$

where $N_+(N_-)$ refers to the number of counts recorded while the fields of the polarimeters were parallel (antiparallel).

Figure 11 and Table VIII give the values of this quantity for the eight regions defined when the pulser was higher than the ^{60}Co peaks and the nine regions when the pulser was lower. The reduced chi-squares (about their means) of the values obtained during the nine pulser-high and six pulser-low three-day-counting sessions (a total of 1000 hours of continuous data taking) are also given.

In a manner analogous to that for the two-detector asymmetry, the dilution and distortion of the single-detector peak asymmetry, A^P, by the background can be removed with the following formula:

$$(1 - f)\ A^P = A^T - fA^B \quad ,$$

where $A^T(A^B)$ is the total (background) asymmetry, and f is the fraction of the total counts in the peak region attributable to the continuous background. The asymmetry of the background was obtained by a least-squares fit of a first degree polynomial in energy to the observed asymmetries in the background regions. This was done in two ways. One procedure was to fit the background region asymmetries independently for the two pulser energy settings. The background asymmetries in the peak regions were removed from the total peak region asymmetries to yield the peak asymmetries which were then combined. The second procedure was to fit the background asymmetries for the two pulser positions with the same function, combine the total asymmetry of the peak regions for the two positions, and then remove the fitted background asymmetry from the total asymmetry to obtain the peak asymmetries. The inputs and results for both

of these methods are displayed in Table IX.

The nonzero asymmetry remaining in the two pulser peaks clearly reveals the presence of a null shift asymmetry. Such a null asymmetry can be understood if we consider the effect of the total count rate asymmetry on the loss of counts from a peak caused by dead time and pulse pileup. These losses will increase as the count rate goes up so that a peak with no true asymmetry will appear to have an asymmetry equal to minus the true total asymmetry of the entire spectrum, A_S^T, times the fraction of counts lost, g. An observed asymmetry will be the sum of the true asymmetry and this null shift asymmetry,

$$A^O = A - g\, A_S^T \quad .$$

If the observed asymmetry is that of the entire spectrum, A_S^O, an expression for the null shift, A^N, is obtained,

$$A^N = -g\, A_S^T = -\frac{f}{1-f} A_S^O \quad .$$

The observed losses were about 0.34 as noted above; if we take 4×10^{-4} as the total observed count rate asymmetry, we find $A^N = -2 \times 10^{-4}$ in rough agreement with the asymmetry observed for the pulser peaks.

By fitting the pulser peak asymmetries with either a constant or linear function, the null shift asymmetry may be determined and then subtracted from the observed peak asymmetries. The resulting true asymmetries are equal to the square of the analyzing power of the polarimeters for the gamma rays of the energy of those peaks. The theoretical expression for the analyzing power, $\eta = -S_e \rho_e \sigma_c L$ allows us to extrapolate these results to the energy of interest, 1081 keV, and

to determine the sign of the analyzing power. Application of the two functional forms of the null shift asymmetry to the results of the two methods of background asymmetry subtraction yields the four values given in Table X. All four values are remarkably consistent. We will adopt the value $\eta_{1.081} = (1.88 \pm 0.05) \times 10^{-2}$ for use in analyzing the ^{18}F measurement.

This value is in reasonable agreement with the calculated value $(1.82 \pm 0.08) \times 10^{-2}$, derived earlier. However, if the value of $\overline{B}_z/B_o$ of 0.17 suggested by Chesler (1965) had been used, the calculated analyzing power would have been 1.73×10^{-2}, in clear disagreement with the measured value. Since the end plate effectiveness ratio given by Chesler was arrived at by fitting experimentally determined analyzing powers, this discrepancy is surprising. It seems possible that no correction for a null asymmetry was made in the experimental measurements done by Chesler; if this is indeed the case, the method given here for determining the end plate correction to the analyzing power of a polarimeter should be preferred.

B. Rotation and Precession of the 937 keV State

Any mechanism that can mimic the effect of a circular polarization must be fully investigated if we are to have confidence in the results of the circular polarization measurements. One such mechanism is a shift in the definition of the zero angle, correlated with the data routing, for radiation with an anisotropic angular distribution. Such an effect could be produced by rotation of the beam direction and/or precession of the excited nucleus in the stray field of the polarimeters.

From Figure 1 it can be seen that the 937 keV gamma ray is especially susceptible to such a problem because it is likely to have an anisotropic angular distribution, and the 937 keV state is fed by the long-lived 5^+ state at 1122 keV.

The asymmetry caused by the beam rotation in a given magnetic field can be calculated if we know the angular distribution of the gamma rays in question (937 keV). The calculation of the precession effect is more complex because it requires a knowledge of the g-factor and lifetime of the precessing state (mainly the 1122 keV state) and, because the 937 keV state is populated both directly and by a cascade, the relative populations of the two states and the angular distributions of the 937 keV gamma-ray as directly produced and as produced by the cascade decay.

B.1 Experimental Procedure

The ONR-CIT tandem Van de Graaff accelerator provided a 150 nanoampere beam of singly-charged ^3He ions at an energy of 4.0 MeV. Two different pressed-Bi_2O_3-powder targets in brass molds were used. One was covered by a 750 nanometer nickel foil, and the other had a 1000 nanometer foil epoxied over it. These targets provided good approximations to the flowing water target system used in the circular polarization measurement without the complications of the vacuum safety system employed for the circular polarization measurement.

Gamma rays were detected in one of the 75 cc Ge(Li) detectors used in the polarization part of the experiment. Pulse height spectra were taken at several backward angles and at 0°, for integrated beam currents of 120 microcoulombs. Peak areas were determined for the 184 keV gamma

ray from the 5^+, T = 0 state at 1122 keV to the 3^+, T = 0 state at 937 keV, the 937 keV gamma ray from the 3^+, T = 0 state to the ground state, and the 1081 keV gamma ray transition from the 0^-, T = 0 level to the ground state. This last-named gamma ray served as a normalizer to correct for variations in solid angle, deadtime and beam current integration between runs. At zero degrees, the brass target holder prevented the 184 keV gamma ray from being observed.

The relative efficiency of the detector over this energy regime was determined by using the 160.6, 223.2, 276.4 and 383.9 keV lines from a ^{133}Ba radioactive source, and the 569.7 and 1063.6 keV lines from a ^{207}Bi source. At zero degrees only the second source was needed to determine the relative efficiency of the 937 keV and 1081 keV gamma rays as seen through the brass target molds.

B.2 Results

These data points and a least-square fit with the first three even Legendre polynomials are graphed in Figure 12. The parameters of the four fits are given in Table XI where the a_o component of the 937 keV angular distribution has been normalized to unity for each of the two target types. It is evident that there is little difference between the results for the two foil thicknesses, and we may therefore restrict our discussion to the 750 nanometer foil case.

B.3 Asymmetry Calculation

The rotation, $\Delta\theta$, induced by a magnetic field, $\vec{B}$, in a beam of charge, q, mass, m, and velocity, $\vec{v}$ is

$$\vec{\Delta\theta} = \frac{q\vec{v}}{mv^2} \times \int \vec{B}\, dr = (3.99 \frac{\text{rad}}{\text{tesla m}}) \frac{\vec{v}}{v} \times \int \vec{B}\, dr \quad .$$

In numerical terms,

$$\Delta\theta = (-3.99 \text{ rad tesla}^{-1}\text{m}^{-1}) \int B_z\, dr \quad ,$$

where q, m, and v have been evaluated for the case of interest. In this experiment we are only concerned with the change in θ between one sense of the magnetization of the polarimeters and the other; the stray field in the minus route may thus be defined as zero. Furthermore, we will define a vertical field as being positive if it points upward. With these conventions, a positive vertical magnetic field will induce a clockwise rotation of the beam direction (zero angle for the angular distribution) as seen from above. If we let the normalized angular distribution be $W(\theta)$, the counts seen in the two counters become

$$L_+ = N_L W(100° - \Delta\theta) \quad , \qquad R_+ = N_R W(100° + \Delta\theta) \quad ,$$

$$L_- = N_L W(100°) \quad , \qquad R_- = N_R W(100°) \quad ,$$

where N_L and N_R are the normalization constants for the two counters. These values for the counts in each detector during each route can be substituted into the definition of the asymmetry. If the Lengendre polynomials are expanded about 100°, the following expression for the asymmetry, A, results:

$$A = -(0.76 \text{ tesla}^{-1}\text{m}^{-1}) \int B_z\, dr \quad .$$

For the horizontal stray fields we found (see Chapter III, Section D) that a typical value for the integral of B was $\sim$50 gauss cm. If we divide this by ten to get an estimated upper limit for the vertical field

value, the asymmetry = $\pm 0.4 \times 10^{-5}$ where the uncertainty in sign results from our lack of knowledge about the vertical field.

The precession of a magnetic dipole $\vec{\mu}$ in a magnetic field $\vec{B}$ during a time Δt is given by

$$\Delta\vec{\theta} = \frac{\vec{\mu} \times \vec{B}}{\left|\vec{J} \times \vec{B}/|B|\right|} \Delta t \quad ,$$

where $\vec{J}$ is the angular momentum associated with the dipole. For a nucleus, $\vec{\mu} = g\mu_N \vec{j}$, where g is the nuclear g-factor for the 1.122 MeV state of ^{18}F (measured by Poletti and Fossan 1967, as $+0.568 \pm 0.013$), μ_N is the nuclear magneton, and $\vec{j} = \vec{J}/\hbar$. The average Δt for an exponentially decaying state is just the exponential decay time τ. With the same conventions as for the beam rotation case, we see that a positive, vertical magnetic field will cause a clockwise precession of the zero angle point of the 187 keV gamma ray's angular distribution, given by

$$\Delta\theta_z = \frac{g\,\mu_N}{\hbar} \tau \frac{\vec{j} \times \vec{B}}{\left|\vec{j} \times \vec{B}/|B|\right|} = (-6.13 \text{ rad tesla}^{-1})\, B_z \quad .$$

The angular distribution of the portion of the 937 keV state which is part of the $5^+ \rightarrow 3^+ \rightarrow 1^+$ cascade can be determined from the formalism of Rose and Brink (1967). As a "stretched" E2, the 937 keV gamma ray angular distribution is the same as for the 187 keV gamma ray, $W_{187}(\theta)$. As before, the counters see

$$L_+ = W_{937}(100°) - W_{187}(100°) + W_{187}(100° - \Delta\theta)$$

$$R_+ = W_{937}(100°) - W_{187}(100°) + W_{187}(100° + \Delta\theta)$$

$$L_- = W_{937}(100°)$$

$$R_- = W_{937}(100°) \quad .$$

These values substituted into the asymmetry ratio will yield, after expanding about 100°: $A = -(0.078\ \text{tesla}^{-1})B_z$. From Chapter III, Section D, we know that 10 gauss was a typical value for the horizontal field at the target so, if the vertical magnetic field is again taken to be $\leq$ one-tenth this, $|A| \leq 0.8 \times 10^{-5}$. Since both precession and beam rotation effects occur simultaneously and with the same sign, we find that $|A| \leq 1.2 \times 10^{-5}$ for the 937 keV gamma ray. This is at least five times smaller than the observed asymmetry of the 937 keV peak; however, given the uncertainty in the actual value of the vertical magnetic field, it still seems prudent to exclude this peak from the process of extracting the circular polarization of the 1081 keV gamma ray.

C. Pulser and ^{60}Co Tests

In order to ensure that no false asymmetry was introduced into the data by the detection and acquisition system, a program of tests was undertaken utilizing an electronic pulse generator and a radioactive ^{60}Co gamma ray source. By concentrating all its counts in a single peak and providing a constant rate of pulses, the pulse generator allowed rapid checks to be made of the amplifiers, sequencer, ADC, and multichannel analyzer system. Although more time-consuming, the radioactive source provided a closer simulation of the beam bombardment situation and included the polarimeters and the Ge(Li) crystals in the test.

For the pulser tests, the output pulses from the pulse generator were fed into the test inputs of the two Ge(Li) detectors. The rest of the acquisition system was set up in the same manner as for the ^{18}F measurement.

The pulse rate was set at approximately 10 kHz, allowing useful count totals to be accumulated in about ten minutes. Tests were conducted with the polarimeters powered and unpowered, with the polarimeter leads in the normal and reversed positions, and with the pulses routed into the lower half and the upper half of the analyzer memory during the plus portion of the cycle. The results of these tests are all consistent with no asymmetry at the level of about one part in a million for both of the aquisition systems used during the course of this experiment. However, the ND4420 system showed apparently random differences in the count totals which could not be accounted for in terms of either the beat frequency between the pulser and the sequencer or the random pulse-pileup and dead time loss due to the room background in the Ge(Li) detectors. This problem was traced to the optical display system by suppressing the display function during the pulser tests. Worry about this problem led to the adoption of the second acquisition system which did not exhibit any problems in the pulse generator tests.

The setup for the radioactive ^{60}Co source tests was identical to that used in the ^{18}F circular polarization measurement except that the water target cell was replaced with a 7 milliCurie ^{60}Co source resting in a lead holder. An appendage on the holder matched the dimensions of the nickel foil holder and was inserted into the beam pipe to position the source at the location of the target spot.

Pulse height spectra were accumulated during four test sessions. Test session one was done with the polarimeter leads in their normal

position and the pulses routed into the lower half of the memory during the plus portion of the cycle. Test session two was done with the polarimeter leads reversed (and thus the routing was also reversed since the definition of the plus half relative to the sequencer is reversed). The conditions for test session three were identical to those in session two. During test session four, the polarimeter leads were in their normal position but the routing was maintained in the state where the upper half of the analyzer memory was used during the plus half of the cycle. Two peak regions, one including the 1.17 MeV gamma ray peak and the other including the 1.33 MeV peak, and four background regions, one above and one below each of the two peaks, were defined and summed by the same computer program as used to analyze the ^{18}F data.

The experimental asymmetries for the six regions during the four test sessions are given in Table XII. The averages for each of the regions as well as the chi-squares about zero, reduced by the four degrees of freedom, are also listed in Table XII. For all 24 values the average asymmetry is $A = (0.05 \pm 1.08) \times 10^{-5}$ with a reduced (24 degrees of freedom) chi-square about zero of 0.90. There is a 60% chance that a Gaussian distribution would give an equal or larger chi-square; thus, there is no evidence for a false asymmetry introduced by the polarimeters, detectors, data-accumulation, or data-processing systems at a level of one part in 10^5.

D. Enhanced Magnetic Field Tests

One of the principal sources of worry about false asymmetries is the stray magnetic field from the polarimeters. Because the target

station was constructed from nonferrous materials, the effect of this field on the beam and target can be studied by artificially enhancing the stray field with current-carrying coils placed on the beam line and powered in synchronism with the polarimeters. This allows two checks to be made: 1) Are the important magnetic field sources of fake asymmetry known and understood? and 2) Are the field induced asymmetries troublesome to the ^{18}F circular polarization measurement if the observed results are scaled by the ratio of the fields?

The synchronously-switched, stray magnetic field can produce false asymmetries through beam rotation, nuclear precession and beam displacement. The expected effects of rotation and precession on the 937 keV state asymmetry have already been discussed in Chapter V, Section B. The principal effect of displacement is expected to be the change in intensity caused by the displacement toward or away from a given counter. If the target is taken as the origin, with the z-axis upward and the x-axis aligned with the incoming beam and pointing downstream, a displacement in the y-direction, Δy, during the plus route will result in an asymmetry $A = -\Delta y/Y$, where Y, for unscattered gamma rays, is the distance between detector and target (the small correction, $\cos 10° = 0.98$, for the placement of the counters at 100° has been ignored). For gamma rays undergoing scattering in the polarimeters, the determination of Y is more complicated. If the case of a thin slab of scattering material between the detector and the target is considered, it is clear that the illumination of the slab determines the intensity variation seen in the detector. Thus, Y for the background is a complicated average over the length of the polarimeter, the interaction

cross section, and the energy spectrum of the gamma rays, which can be roughly approximated by one-half the detector to target distance.

The magnetic field induced displacement, Δy, is given by

$$\Delta y = -\frac{qv_x}{mv^2}\int B_z|x|dx = -(3.99\ \text{tesla}^{-1}\text{m}^{-1})\int B_z|x|dx \quad ,$$

where q, m, and v are defined in Chapter V, Section B. The detector to target distance is 0.216 meters, so the peak asymmetry should be

$$A^p = +\ (18.5\ \text{tesla}^{-1}\text{m}^{-2})\int B_z|x|dx \quad .$$

The tests were conducted with the same experimental equipment and procedure used in the polarization measurement, except that either of two sets of modified Helmholtz coils was positioned along the beam line upstream of the target, and powered in series with the polarimeter. One set of coils, consisting of two 12.8 cm by 2.6 cm rectangles, each containing 20 turns of number 12 wire, was placed on either side of the beam line, 2.5 cm apart in the region between the target and the aperture downstream of the cold trap (see Figure 2). Test sessions were conducted with the coils oriented to enhance the vertical field or oriented to enhance the horizontal field. The second set of coils, in the form of two 15.2 cm × 5.7 cm rectangles, each containing 4 turns of wire, was placed in the region between the two fast-acting vacuum valves, approximately 0.75 meters from the target. The two coils were separated by 6.4 cm and oriented to give either a vertical or a horizontal field enhancement.

The results for the asymmetry of the 5 background and the 5 peak regions, defined in the ^{18}F pulse-height spectrum, during the four test

situations (near and far field enhancement in the vertical and horizontal directions) are presented in Table XIII and Table XIV. Because the principal sources of background asymmetry are expected to be energy independent, the average of the five background regions has been used as the background asymmetry to be removed from the peak-region asymmetry to obtain the peak asymmetries listed in Table XV.

The vertical enhancement of the near field resulted in a field at the target of $B_z = 40.7$ Gauss, a field integral of $\int B_z dx = 304$ Gauss-cm, and a distance weighted integral of $\int B_z |x| dx = 1144$ Gauss-cm^2. Thus, we expect a background asymmetry, $A^B = (+4.1) \times 10^{-4}$, a peak asymmetry, $A^P = (+2.1) \times 10^{-4}$, except for the 937 keV peak where $A^P = (-3.2 - 2.3 + 2.1) \times 10^{-4} = (-3.4) \times 10^{-4}$. These predictions, however, ignore the effect of the dead time and pulse pileup on the observed asymmetries. The asymmetry of the total energy spectrum is dominated by the background asymmetry, so the loss of 25% of the background counts from dead time (pile-out is approximately balanced by pile-in for the large, flat background regions) means a background null shift $A_N^B = (-1.0) \times 10^{-4}$ and an observed background asymmetry $A_o^B = (+3.1) \times 10^{-4}$, which agrees well with the experimental value of $(+3.6 \pm 0.6) \times 10^{-4}$. Similarly, the loss of 50% of the counts from the peaks will result in a null asymmetry of $A_N^P = (-2.1) \times 10^{-4}$ and an expected, observed asymmetry of $A_o^P = (0.0) \times 10^{-4}$, except for the 937 keV peak where $A_o^P = (-5.5) \times 10^{-4}$. Again, these predictions are in excellent agreement with the experimental values given in Table XV for the present experimental situation. (It is interesting to note the

fortuitous cancellation of the displacement induced asymmetry in the peaks due to the combination of a 50% loss rate in the peaks and a doubling of the true background asymmetry over that of the peaks because the background arises from scattering at about half the distance to the target.) Finally, these results can be scaled down by the ratio of the fields ($\simeq$ 100) to yield asymmetries for the polarization measurement which are negligible at the present level of statistical uncertainty.

The next test was conducted with the same field enhancement coils, rotated 90° to give an enhanced field in the $-\hat{y}$ direction during the plus route. Unfortunately, magnetic field measurements made following the test indicated a slight enhancement of the vertical field as well, $B_z = 0.5G$, $\int B_z dx = 65.3$ G-cm and $\int B_z \, x \, dx = 371$ G cm^2. These field values indicate a need to correct the observed background asymmetry, $A_o^B = (1.01 \pm 0.65) \times 10^{-4}$, by $A^B = (1.00) \times 10^{-4}$ to yield $A_o^B = (0.01 \pm 0.65) \times 10^{-4}$. The 937 keV peak asymmetry, $A_o^P = (1.78 \pm 2.92) \times 10^{-4}$, must be corrected by $A^P = (-0.50) \times 10^{-4}$ to give $A_o^P = (2.72 \pm 2.92) \times 10^{-4}$. After these corrections, the asymmetry values are all completely consistent with zero. The average peak asymmetry, $\bar{A}^P = (-1.22 \pm 1.53) \times 10^{-4}$ can be reduced by the field ratio, ~ -10, to yield a predicted asymmetry in the polarization measurement situation which is consistent with zero only to within an error approximately as large as the present level of statistical uncertainty.

The enhancement of the stray field far upstream from the target, as done in the remaining two test situations, introduces a new

complication into the asymmetry-producing effects of displacement and rotation; most of the beam rotation and displacement occur before the beam is collimated by the beam defining aperture (see Figure 2). The displacement of the beam on this aperture causes intensity variations and movement of the center of gravity of the beam spot, which are functions of the beam spot structure. With this dependence on the beam spot structure, it becomes impossible to predict the induced asymmetry.

However, the observed asymmetries may still be scaled by the field ratios to give an indication of the seriousness of this mechanism for the polarization measurement. The enhanced field was approximately 5 Gauss in the region of the enhancement coils, $\int B\,dx \simeq 74.5$ Gauss-cm and $\int B|x|dx \simeq 2600$ Gauss cm^2 (the actual integral was 5600 Gauss-cm^2, but the aperture hides the upstream beam displacements, and only the upstream rotation times the aperture-to-target distance matters). The enormous distance-weighted enhanced field produced a target spot movement clearly visible in the television monitor. For the vertical field enhancement, this represents a field ratio of approximately 10,000. The experimental asymmetries in Tables XIII and XV are totally negligible when reduced by this factor. The horizontal field enhancement ($\sim$1000) will also predict asymmetries too small to matter at the current level of statistical precision for the conditions of the circular polarization measurement.

Thus, we have found that, with the possible exception of the horizontal field close to the target, the observed enhanced-field asymmetries, reduced by the enhancement factors, indicate no significant

problems in the circular polarization measurement. Our success in predicting the experimental asymmetries of the vertical field enhancement close to the target leads us to believe that we understand the effects of the magnetic field in the neighborhood of the target, and therefore that no unsuspected mechanisms caused by the horizontal field close to the target will produce an asymmetry large enough to cause trouble in the circular polarization measurements.

REFERENCES

Abbott, L. F. and Barnett, R. M. 1978, Phys. Rev. Lett. 40, 1303.

Adelberger, E. G. et al. 1975, Phys. Rev. Lett. 34, 402.

Ajzenberg-Selove, F. 1972, Nucl. Phys. A190, 1.

Benvenuti, A. et al. 1974, Phys. Rev. Lett. 32, 800.

Box, M. A. et al. 1976, J. of Phys. G8, L107.

Cabibbo, N. 1963, Phys. Rev. Lett. 10, 531.

Chemtob, M. and Desplanques, B. 1974, Nucl. Phys. B78, 139.

Chesler, R. B. 1965, Nucl. Inst. and Meth. 37, 185.

Desplanques, B. and Hadjimichael, E. 1976, Nucl. Phys. B107, 125.

Desplanques, B. and Micheli, J. 1977, Phys. Lett. 68B, 339.

Donoghue, J. 1976, Phys. Rev. D13, 2064.

Feynman, R. P. and Gell-Mann, M. 1958, Phys. Rev. 109, 193.

Fischbach, E. and Tadić, D. 1973, Phys. Reports 6C, 124.

Galić, H. and Tadić, D. 1976, Fisika 8, 99.

Gari, M. 1973, Phys. Reports 6C, 317.

Gari, M. 1977, Ruhr-Universität Bochum Report No. RUB/TPII/163 (to be published).

Gari, M., McGory, J. B., and Offermann, R. 1975, Phys. Lett. 55B, 277.

Gari, M. and Reid, J. H. 1974, Phys. Lett. 53B, 237.

Glashow, S. L., Iliopoulos, J., and Maiani, L. 1970, Phys. Rev. D2, 1285.

Hasert, F. J. et al. 1973, Phys. Lett. 46B, 121.

Henley, E. M. 1968, Phys. Lett. 28B, 1.

Hung, P. Q. and Sakurai, J. J. 1977, Phys. Lett. 69B 323

Körner, J. G. 1973, Phys. Lett. 44B, 361.

Lobashov, V. M. et al. 1972, Nucl. Phys. A197, 241.

Neubeck, K., Schober, H., and Wäffler, H. 1974, Phys. Rev. C10, 320.

Pirner, H. J. and Riska, D. D. 1973, Phys. Lett. 44B, 151.

Poletti, A. R. and Fossan, D. B. 1967, Phys. Rev. 160, 883.

Rose, H. J. and Brink, D. M. 1967, Rev. Mod. Phys. 39, 306.

Salam, A. 1968, in Elementary Particle Theory, edited by Svartholm, N. (Almqvist and Wiksell, Stockholm, 1968), p. 367.

Schülke, L. 1972, Nucl. Phys. B40, 386.

Wambach, U. M., Gari, M., and Kümmel, H. 1970, Phys. Lett. 33B, 253.

Weinberg, S. 1967, Phys. Rev. Lett. 19, 1264.

Weinberg, S. 1972, Phys. Rev. D5, 1412.

Table I

Chronology of the data-taking sessions. Column 1 lists the dates during which the data were taken, grouped into the fifteen sessions numbered in column 2. Changes or improvements in the experiment are noted in column 3.

Table I: CHRONOLOGY

Date	Session No.	Notes
17-23/9/75, 10-12/10/75	1	
22-27/11/75	2	Second set of polarimeters installed
10-16/12/75	3	
26-30/5/76	4	ND4420 display suppressed
11-12/9,29/9 - 3/10,8-10/10/76	5	Ge(Li)'s redrifted, new analyzers, new beam line
11-15/11/76	6	First set of canceling coils installed
11-15/12/76	7	
20-23/1/77	8	
30-31/1/77	9	
3-9/3/77	10	Second set of canceling coils installed
20-25/3/77	11	Third set of canceling coils installed
1-2/4/77	12	
5-8/5/77	13	
2-16/7/77	14	
25/7 - 2/8/77	15	

Table II

Observed Asymmetries. Column 2 gives the asymmetry (in units of 10^{-4}) for each region listed in column 1 (where B1 through B5 refer to the five background regions, and the peak regions are denoted by their energy in keV) for the periods when the polarimeter-lead polarity switch was in the "normal" position. The uncertainty associated with each value is given directly underneath that value in the same units (10^{-4}). Column 3 lists the reduced chi-square of the results from the individual sessions about the mean given in column 2, for each region. Columns 4 and 5 are similar to 2 and 3, respectively, except they are for the periods when the switch was in the "reverse" position. Columns 6 and 7 are for the total of both positions. All of these results are shown as graphs in Figure 8.

Table II: OBSERVED ASYMMETRIES

	$A_{Nor}(10^{-4})$	Reduced χ^2	$A_{Rev}(10^{-4})$	Reduced χ^2	$A_{tot}(10^{-4})$	Reduced χ^2
B1	0.09 ±0.20	0.60	0.45 ±0.23	1.57	0.24 ±0.15	1.01
937	0.45 ±0.24	0.60	0.49 ±0.29	0.61	0.47 ±0.19	0.58
B2	0.11 ±0.23	0.86	0.22 ±0.27	0.97	0.15 ±0.18	0.88
1020	0.23 ±0.39	0.58	0.81 ±0.48	1.49	0.46 ±0.30	0.95
1042	-0.56 ±0.29	2.09	0.09 ±0.35	1.23	-0.29 ±0.23	1.75
B3	-0.42 ±0.49	1.41	0.04 ±0.56	0.75	-0.22 ±0.37	1.11
1081	-0.07 ±0.32	0.99	-0.08 ±0.39	1.16	-0.07 ±0.24	1.01
B4	-0.15 ±0.27	1.27	0.18 ±0.32	0.88	-0.01 ±0.21	1.09
1164	0.06 ±0.41	1.91	-0.26 ±0.51	0.87	-0.07 ±0.32	1.43
B5	-0.13 ±0.28	0.92	0.16 ±0.33	1.92	-0.01 ±0.21	1.29

Table III

^{18}F Background Fits. Three least-square fits of polynomials in E to the asymmetries of the five background regions are presented. The kind of fitting function is identified in column 1. The coefficients of the fits are given in columns 2 through 4. Column 5 gives the chi-square of the fits divided by the appropriate number of degrees of freedom (4,3,2). It should be noted that the errors on the coefficients are correlated; thus it is necessary to employ the whole error matrix to obtain the standard error for the asymmetries predicted by these fits.

Table III: ^{18}F BACKGROUND FITS

Type	$a_o(10^{-5})$	$a_1(10^{-5})$	$a_2(10^{-5})$	Reduced χ^2
constant	1.03 ± 0.88	-	-	0.561
linear	-1.06 ± 0.78	0.94 ± 0.76	-	0.230
quadratic	58.1 ± 100.4	-101.8 ± 194.9	44.4 ± 93.6	0.236

Table IV

^{18}F Background Subtractions. For the five peaks listed in column 1, the three background-asymmetry functions given in Table III are evaluated in columns 3 through 5. By using the formula $(1-f)A^P = A^T - fA^B$, the three background values may be subtracted from the total peak-region asymmetry given in column 2 to yield the peak asymmetries given in columns 7 through 9. The value of f is given in column 6 for each peak.

Table IV: ^{18}F BACKGROUND SUBTRACTION

Peak (MeV)	$A^{T}_{o}(10^{-5})$	$A^{B}_{o\,con}(10^{-5})$	$A^{B}_{o\,lin}(10^{-5})$	$A^{B}_{o\,quad}(10^{-5})$	f	$A^{P}_{o\,con}(10^{-5})$	$A^{P}_{o\,lin}(10^{-5})$	$A^{P}_{o\,quad}(10^{-5})$
0.937	4.7	1.03	1.81	1.66	0.3056	6.33	5.97	6.04
	±1.9	±0.88	±1.08	±1.12		±2.76	±2.78	±2.78
1.020	4.6	1.03	1.03	0.42	0.6626	11.67	11.61	12.81
	±3.0	±0.88	±0.88	±1.55		±9.07	±9.07	±9.40
1.042	-2.9	1.03	0.82	0.19	0.3524	-5.02	-4.92	-4.58
	±2.3	±0.88	±0.90	±1.60		±3.59	±3.59	±3.66
1.081	-0.7	1.03	0.45	-0.10	0.3711	-1.70	-1.38	-1.05
	±2.4	±0.88	±1.00	±1.54		±3.85	±3.86	±3.92
1.164	-0.7	1.03	-0.33	-0.28	0.5675	-2.93	-1.19	-1.25
	±3.2	±0.88	±1.41	±1.41		±7.49	±7.63	±7.63

Table V

^{18}F Peak Null Fits. Two least-squares fits have been made to each of the three peak asymmetry values for the 1.02, 1.04 and 1.16 MeV peaks given in columns 7 through 9 of Table IV. Column 1 lists the type of background fitting function used to obtain the peak asymmetries. Column 3 gives the result for the null shift of the 1.08 MeV peak of fitting the peak asymmetries with a constant. Column 4 gives the reduced chi-squares of these three fits and, in parentheses, the reduced chi-squares of the fitted peaks about zero. Similarly, columns 5 and 6 give the null shift for the 1.08 MeV peak and the chi-square (one degree of freedom) when the three peak asymmetry values given for each of the three background fits are fitted with a linear function. The null shift values of the constant and linear fits are subtracted from the observed asymmetry of the 1.08 MeV peak given in column 2 to yield the "true" asymmetries given in columns 7 and 8, respectively.

Table V: ^{18}F PEAK NULL FIT

Type	$A^{P_o}_{1.08}(10^{-5})$	$A^{N}_{con}(10^{-5})$	Reduced χ^2	$A^{N}_{lin}(10^{-5})$	χ^2	$A^{P}_{1.08}(10^{-5})$	$A^{P}_{1.08}(10^{-5})$
constant	-1.70	-2.79	1.46	-3.16	2.85	1.09	1.46
	±3.85	±3.05	(1.26)	±3.35		±4.91	±5.10
linear	-1.38	-2.44	1.45	-2.55	2.90	1.06	1.17
	±3.86	±3.06	(1.18)	±3.38		±4.93	±5.13
quadratic	-1.05	-2.12	1.49	-2.29	2.97	1.07	1.25
	±3.92	±3.11	(1.15)	±3.41		±5.00	±5.20

Table VI

^{18}F Null-Only Fits. The asymmetries of the 5 background regions and the 1.02, 1.04 and 1.16 MeV peak regions (all given in column 6 of Table II) were used to make three least-square fits of the types of polynomial in E listed in column 1. The results of these fits for the null shift of the 1.08 MeV peak are given in column 3, and the reduced chi-squares of the fits are given in column 4. The null shifts are subtracted from the observed total asymmetry of the 1.08 MeV peak region given in column 2 to yield the "true" total asymmetry of column 5. The effect of the background is removed by using the expression $(1-f)A^P = A^T - fA^B$ where f is given in column 6 and A^B is, by assumption, identically zero. This procedure yields the "true" peak asymmetries listed in column 6.

Table VI: NULL ONLY FITS

Type	$A^{T_o}(10^{-5})$	$A^N(10^{-5})$	Reduced χ^2	$A^T(10^{-5})$	f	$A^P(10^{-5})$
constant	0.7	0.74	0.960	-1.44	0.3711	-2.29
	±2.4	±0.77		±2.52		±4.01
linear	0.7	0.19	0.777	-0.89	0.3711	-1.42
	±2.4	±0.85		±2.55		±4.05
quadratic	-0.7	-0.35	0.839	-0.35	0.3711	-0.56
	±2.4	±1.16		±2.67		±4.24

Table VII

^{18}F Circular Polarization. The "true" 1.08 MeV peak asymmetries in Tables IV (line 2 of this table), V (line 1), and VI (line 3) for the fits with the lowest reduced chi-square are given in column 2. The types of background and null fitting functions used to arrive at the results in column 2 are given in column 1. Dividing column 2 by the analyzing power $(1.88 \pm 0.05) \times 10^{-2}$ yields the circular polarization in column 3. Dividing column 3 by the conventional Cabibbo prediction of 3.6×10^{-4} gives the "enhancement" factors in column 4. Line 2 is the preferred treatment, although the other values are the same within the errors quoted.

Table VII: CIRCULAR POLARIZATION

Type of Fit background	Type of Fit null	$A^P(10^{-5})$	$P_\gamma(10^{-3})$	"Enhancement"
linear	constant	1.06	0.56	1.56
		±4.93	±2.62	±7.28
linear	zero	-1.38	-0.73	-2.03
		±3.86	±2.05	±5.69
zero	linear	-1.42	-0.76	-2.11
		±4.05	±2.15	±5.98

Table VIII

Analyzing power measurement: observed asymmetries. The asymmetries for the regions listed in column 1 are given in column 2 for the runs in which the pulser was set to give a peak at higher energy than the 1332 keV peak, and in column 4 for the time while the pulser peak was set below the 1173 keV peak. Columns 3 and 5 give the reduced chi-squares of the appropriate runs about the results in columns 2 and 4. These asymmetries are displayed in the form of graphs in Figure 11.

Table VIII: ANALYZING POWER OBSERVED ASYMMETRIES

Region	$A_{High}(10^{-4})$	Reduced χ^2	$A_{Low}(10^{-4})$	Reduced χ^2
B1	-	-	3.53 ±0.25	0.10
$Pulser_L$	-	-	-0.56 ±0.30	0.49
B2	-	-	3.94 ±0.26	0.28
B3	4.02 ±0.25	0.84	3.92 ±0.27	0.84
1.17 MeV	3.18 ±0.25	0.96	3.01 ±0.30	1.44
B4	4.88 ±0.40	0.30	5.44 ±0.44	0.94
B5	4.94 ±0.37	0.96	4.67 ±0.45	0.74
1.33 MeV	3.87 ±0.22	1.02	4.10 ±0.27	1.18
B6	7.28 ±0.55	1.30	6.91 ±0.71	1.23
$Pulser_H$	-1.26 ±0.36	0.30	-	-
B7	6.97 ±0.84	0.60	-	-

Table IX

Analyzing power measurement: background asymmetry subtraction. The top three lines of the table detail the results of a linear background least-squares fit to the 6 background regions when the pulser was low. The fitted background asymmetry values of column 3 were removed from the observed total peak region asymmetries of column 2 (identified in column 1) by means of the equation $(1-f)A^P = A^T - fA^B$ where f is given in column 4. This procedure yields the peak asymmetry values given in column 5. Similarly, the next three lines give the results for a least-squares fit to the 5 background regions when the pulser was high. Finally, the last four lines describe the results of a simultaneous fit to all 11 background regions and the subsequent removal of background asymmetries from the peak region asymmetries to yield the peak asymmetries. The three fits are graphed in Figure 11.

Table IX: ANALYZING POWER BACKGROUND SUBTRACTION

Region	$A^T(10^{-4})$	$A^B(10^{-4})$	f	$A^P(10^{-4})$
$Pulser_L$	-0.56	3.67	0.290	-2.29
	±0.30	±0.16		±0.43
1.17_L	3.01	4.56	0.170	2.69
	±0.30	±0.16		±0.36
1.33_L	4.10	5.56	0.050	4.03
	±0.27	±0.31		±0.28
1.17_H	3.18	4.42	0.170	2.92
	±0.25	±0.18		±0.30
1.33_H	3.87	5.90	0.050	3.76
	±0.22	±0.26		±0.23
$Pulser_H$	-1.26	7.04	0.045	-1.65
	±0.36	±0.42		±0.38
$Pulser_L$	-0.56	3.59	0.290	-2.25
	±0.30	±0.14		±0.43
1.17_{Ave}	3.11	4.57	0.170	2.81
	±0.19	±0.11		±0.23
1.33_{Ave}	3.96	5.71	0.050	3.87
	±0.17	±0.19		±0.18
$Pulser_H$	-1.26	6.60	0.045	-1.63
	±0.36	±0.29		±0.38

Table X

Analyzing power measurements: shifts and final values. The peak asymmetries for the two pulser positions permit either a constant or a linear fit for the null shift. These two fits can be made either for the pulser peaks determined by the separate background fits or for the peaks determined by the single fit to all the backgrounds together. The resulting null shift values are given in column 5 for the peaks of column 1 under the conditions listed in columns 2 and 3. Column 5 is subtracted from the appropriate peak asymmetry given in column 4, and the square root is taken of the result to yield the analyzing powers listed in column 6 for the two ^{60}Co peaks. These analyzing powers are then extrapolated to 1.08 MeV in column 7 using the circular-polarization sensitive portion of the Klein-Nishina cross section as a guide. The results of the extrapolation from the two peaks are averaged in column 8.

Table X: ANALYZING POWER NULL SHIFTS AND FINAL VALUES

Region	Background Fit	Null Fit	$A^P(10^{-4})$	$A^N(10^{-4})$	$\eta(10^{-2})$	$\eta_{1.08}(10^{-2})$	$\bar{\eta}_{1.08}(10^{-2})$
1.17	separate	constant	2.83 ±0.23	-1.93 ±0.29	2.182 ±0.084	1.940 ±0.075	
							1.883 ±0.044
1.33	separate	constant	3.87 ±0.18	-1.93 ±0.29	2.408 ±0.070	1.854 ±0.054	
1.17	separate	linear	2.83 ±0.23	-2.08 ±0.32	2.217 ±0.088	1.970 ±0.078	
							1.884 ±0.045
1.33	separate	linear	3.87 ±0.18	-1.84 ±0.30	2.389 ±0.073	1.839 ±0.056	
1.17	together	constant	2.81 ±0.23	-1.90 ±0.28	2.171 ±0.085	1.930 ±0.075	
							1.877 ±0.044
1.33	together	constant	3.87 ±0.18	-1.90 ±0.28	2.402 ±0.070	1.850 ±0.054	
1.17	together	linear	2.81 ±0.23	-2.06 ±0.32	2.208 ±0.089	1.963 ±0.079	
							1.880 ±0.046
1.33	together	linear	3.87 ±0.18	-1.83 ±0.30	2.387 ±0.073	1.838 ±0.056	

Table XI

Angular distribution coefficients. Least-square fits of an expansion in even Legendre polynomials up to fourth order have been made for the angular distribution measurements shown in Figure 12. The gamma ray energies and the foil thicknesses traversed by the beam are listed in columns 1 and 2. The expansion coefficients are listed in columns 3 through 5, where the a_o coefficient of the 937 keV gamma ray is normalized to unity.

Table XI: ANGULAR DISTRIBUTION COEFFICIENTS

Gamma Ray	Foil (Å)	a_o	a_2/a_o	a_4/a_o
184	7500	0.083	0.337	-0.074
937	7500	1	0.232	-0.171
184	10000	0.082	0.257	-0.037
937	10000	1	0.234	-0.078

Table XII

^{60}Co source tests: region asymmetries for the four background regions and the two peaks (listed in column 1) are given for each of the four test situations in columns 2 through 5. The average of the four tests and the reduced chi-squares of the tests about that average are given in columns 6 and 7. The weighted mean of all 24 values and the reduced chi-square about that value are given at the bottom of columns 6 and 7. Test situations are described on page 57.

Table XII: ^{60}Co SOURCE TESTS: REGION ASYMMETRY (10^{-5})

Region	Test 1	Test 2	Test 3	Test 4	Total	Reduced χ^2 about 0
B1	-3.85	4.39	-4.89	4.97	0.21	1.22
	±3.89	±3.20	±4.27	±5.85	±2.01	
1.17 MeV	1.90	7.85	1.20	2.28	3.97	1.05
	±4.84	±3.98	±4.79	±6.90	±2.42	
B2	-0.13	0.07	-11.41	-5.89	-4.19	1.23
	±6.12	±5.16	±5.53	±7.32	±2.94	
B3	-4.73	-8.81	-2.64	-9.45	-6.27	1.22
	±6.51	±5.35	±5.92	±7.85	±3.11	
1.33 MeV	4.23	0.98	5.13	-0.88	2.64	0.49
	±4.90	±4.03	±4.84	±7.04	±2.45	
B4	2.05	-4.01	-1.33	7.35	0.13	0.21
	±9.80	±8.05	±7.80	±10.33	±4.40	
				Average	0.05 ±1.08	0.90

Table XIII

Enhanced magnetic field tests: observed background region asymmetries. The asymmetries of the background regions listed in column 1 are given in columns 2 through 5 for each of the four test conditions described in the text, page 60 . The weighted mean of the five regions for each test condition is given at the bottom of columns 2 through 5.

Table XIII: ENHANCED MAGNETIC FIELD TESTS

OBSERVED BACKGROUND REGION ASYMMETRIES (10^{-4})

Region	Test 1	Test 2	Test 3	Test 4
B1	3.26	1.99	5.42	-2.56
	±1.16	±1.15	±1.06	±1.06
B2	3.88	0.39	7.36	-1.64
	±1.32	±1.30	±1.31	±1.31
B3	2.28	0.61	5.31	-0.37
	±2.47	±2.46	±2.51	±2.50
B4	3.59	1.37	6.93	-1.50
	±1.54	±1.52	±1.51	±1.50
B5	4.40	-0.14	6.10	0.13
	±1.58	±1.57	±1.50	±1.49
Averages	+3.61	+1.01	+6.25	-1.55
	±0.66	±0.65	±0.63	±0.63

Table XIV

Enhanced magnetic field tests: observed peak region asymmetries. The observed asymmetries of the five peak regions listed in column 1 are given in columns 2 through 5 for each of the four test conditions.

Table XIV: ENHANCED FIELD TESTS

OBSERVED PEAK REGION ASYMMETRIES (10^{-4})

Region	Test 1	Test 2	Test 3	Test 4
0.937 MeV	-2.48	1.39	-0.91	-0.06
	±1.44	±1.41	±1.38	±1.37
1.020 MeV	3.00	0.57	0.89	-0.33
	±2.44	±2.40	±2.33	±2.32
1.042 MeV	1.19	-1.65	-1.68	1.05
	±1.77	±1.74	±1.68	±1.67
1.081 MeV	0.04	-1.16	-2.28	-1.77
	±1.90	±1.87	±1.86	±1.85
1.164 MeV	5.79	-0.59	0.72	-2.44
	±2.71	±1.57	±2.46	±2.73

Table XV

Enhanced magnetic field tests: observed peak asymmetries. The effect of the average background asymmetries given at the bottom of columns 2 through 5 of Table XIII have been removed from the peak region asymmetries of Table XIV by means of the equation $(1-f)A^P = A^T - fA^B$, and the values of f given in column 2 of this table. This procedure yields the observed peak asymmetries given in columns 3 through 6 for the peaks listed in column 1 during the four test conditions.

Table XV: ENHANCED FIELD TESTS

OBSERVED PEAK ASYMMETRIES (10^{-4})

Region	f	Test 1	Test 2	Test 3	Test 4
0.937 MeV	0.29	-4.99	1.78	-3.85	0.55
		±2.05	±2.92	±1.97	±1.95
1.020 MeV	0.65	1.85	-0.26	-9.12	1.96
		±7.10	±6.98	±6.79	±6.75
1.042 MeV	0.34	-0.60	-3.04	-5.81	2.40
		±2.71	±2.67	±2.58	±2.56
1.081 MeV	0.36	-1.95	-2.36	-7.02	-1.89
		±2.98	±2.94	±2.92	±2.90
1.164 MeV	0.55	8.46	-2.56	-6.04	-3.54
		±6.08	±5.65	±5.53	±6.12

Supplementary Table

NUCLEON-NUCLEON AND ELECTRON-NUCLEON PARITY NON-CONSERVING EXPERIMENTS
AS OF JULY 1978

The nucleus and transition are listed in columns 1 and 2. Column 3 contains the results of experiments referred to in column 4. For transitions with multiple reported values only the two reports which are the most recent and/or most accurate are listed, except that only one value from a given group is listed. Columns 5 and 6 contain the theoretical values based on the Cabibbo charged-currents only. The same selection rules have been applied to these listings as well. For the convenience of the reader, the reference information is contained in the table itself, rather than the reference list.

Supplementary Table: NN and eN PNC Experiments as of July 1978

Nucleus	Transition	Experimental Value		Theoretical Value* Cabibbo	
		Nucleon-Nucleon			
^{2}H	$n+p \rightarrow d+\gamma$	$P_\gamma = -(1.30\pm0.45)10^{-6}$	Lobashov et al.1972 Nucl. Phys. A197,241	$(2.2\text{-}11.8)10^{-8}$ $(5\text{-}17)10^{-8}$	Lassey & McKellar 1976 Nucl.Phys. A260,413; Epstein 1976 Nucl.Phys. A271,429
		$A_\gamma = (0.6\pm2.1)10^{-7}$	Cavaignac et al.1977 Phys.Lett. 67B,148	$(4\text{-}7)10^{-9}$ $(4.5)10^{-9}$	Lassey & McKellar 1976 Nucl.Phys. A260,413; Desplanques 1975 Nucl.Phys. A242,423
	$\vec{p}+p \rightarrow p+p$	$A_p = (.05\pm1.4)10^{-7}$	Potter et al.1976 ANL Symp.on pol. beams and targets	$(2\text{-}6)10^{-8}$ $-(6)10^{-7}$	Epstein 1975 Phys.Lett. 55B,249; Brown et al.1973 Phys.Rev.Lett.30,770
	$\vec{p}+d \rightarrow p+d$	$A_p = (0\pm1.5)10^{-7}$	Nagle 1977, FNAL Ben Lee Mem. Conf. (to be published)		
^{16}O	$(2^-, 8{,}9$ MeV$) \rightarrow {}^{12}C+\alpha$	$\Gamma_\alpha = (1.0\pm0.3)10^{-10}$eV	Neubeck et al.1974 Phys.Rev. C10,320	$(0.3)10^{-10}$eV $(0.7)10^{-10}$eV	Apagyi et al.1976 Nucl.Phys. A272,317 Gari et al. 1971 Nucl.Phys. A161,625
^{18}F	$0^- \rightarrow 1^+$	$P_\gamma = -(0.6\pm2.0)10^{-3}$	Present work; Barnes et al.1978 Phys.Rev.Lett.40,840	$\pm(3.6)10^{-4}$	Gari et al. 1975 Phys.Lett. 55B,277
^{19}F	$1/2^- \rightarrow 1/2^+$	$A = -(8.5\pm2.5)10^{-5}$	Adelberger 1978 private communication	$(0.7\text{-}1.1)10^{-4}$	Box et al.1976 Nucl.Phys. A271,412

* Only theoretical values published since 1970 are included

Nucleus	Transition	Experimental Value		Theoretical Value Cabibbo	
^{21}Ne	$1/2^- \rightarrow 3/2^+$	$P_\gamma = -(0.9 \pm 5.1)10^{-3}$	Snover et al.1978 Phys.Rev.Lett.41,145	$(1\text{-}26)10^{-3}$	Brandenburg et al.1978 preprint UM-P-78/31
^{41}K	$7/2^- \rightarrow 3/2^+$	$P_\gamma = (1.9 \pm 0.3)10^{-5}$	Lobashov et al.1969 Phys.Lett.30B,39	$-(4)10^{-6}$	Desplanques 1975,Thesé, Université de Paris Sud.
		$A_\gamma = (2.4 \pm 3.6)10^{-3}$	Boehm & Hauser 1960 Nucl.Phys. 14,615		
^{57}Fe	$3/2^- \rightarrow 1/2^-$	$P_\gamma = (2.0 \pm 6.0)10^{-5}$	Kankeleit 1964, Congres Internat.de Physique Nucléaire, Paris, Vol. II, p. 1206		
^{75}As	$5/2^+ \rightarrow 3/2^-$	$P_\gamma = -(1.8 \pm 1.5)10^{-5}$	Kuphal et al.1974 Nucl.Phys. A234,308		
		$P_\gamma = -(6.0 \pm 2.0)10^{-5}$	Vanderleeden et al. 1972, Phys.Rev. C4,2218		
^{114}C	$1^+ \rightarrow 0^+$	$P_\gamma = -(6.0 \pm 1.5)10^{-4}$	Alberi et al. 1972 Phys.Rev.Lett. 29,518		
		$A_\gamma = -(0.6 \pm 1.8)10^{-4}$	Warming 1969 Phys.Lett. 29B,564		
		$A_\gamma = (1.2 \pm 1.2)10^{-4}$	Eichler & Heine 1969 Z.Physik 227,352		
^{118}Sn	$\vec{n}$	$A_\gamma = (4 \pm 0.6)10^{-4}$	R. Wilson 1978 private communication *		
		$A_\gamma = (8.5 \pm 1.5)10^{-4}$	R. Wilson 1978 private communication **		
^{133}Cs	$5/2^+ \rightarrow 7/2^+$	$A_\gamma = (1.5 \pm 1.5)10^{-3}$	Boehm & Hauser 1960 Nucl.Phys. 14,615		

*Unpublished result from I.L.L. Grenoble
**Unpublished result from I.T.E.P. U.S.S.R.

Nucleus	Transition	Experimental Value		Theoretical Value Cabibbo	
^{159}Tb	$5/2^- \rightarrow 3/2^+$	$P_\gamma = -(1.0\pm5.0)10^{-4}$	Lipson et al.1972 Phys.Rev. C5,932		
		$A_\gamma = -(3.0\pm4.3)10^{-4}$	Krane et al.1971 Phys.Rev. C4,1942		
		$A_\gamma = (4.5\pm3.0)10^{-4}$	Pratt et al.1970 Phys.Rev. C2,1499		
	$5/2^+ \rightarrow 3/2^+$ (348 keV)	$A_\gamma = (1.7\pm5.0)10^{-3}$	Krane et al.1971 Phys.Rev. C4,1942		
	$5/2^+ \rightarrow 3/2^+$ (226 keV)	$A_\gamma = -(1.2\pm4.0)10^{-3}$	Krane et al.1971 Phys.Rev. C4,1942		
^{161}Dy	$3/2^- \rightarrow 5/2^-$	$A_\gamma = -(3.0\pm3.2)10^{-3}$	Krane et al.1971 Phys.Rev. C4,1942		
	$3/2^- \rightarrow 5/2^+$	$A_\gamma = -(0.2\pm2.0)10^{-3}$	Krane et al.1971 Phys.Rev. C4,1942		
^{171}Tm	$7/2^- \rightarrow 7/2^+$	$P_\gamma = (0.8\pm1.5)10^{-4}$	Kuphal et al.1974 Nucl.Phys. A234,308		
^{175}Lu	$9/2^- \rightarrow 7/2^+$	$P_\gamma = (5.7\pm0.8)10^{-5}$	Kuphal et al.1974 Nucl.Phys. A234,308	$-(1)10^{-5}$	Desplanques 1975, Thesé, Université de Paris Sud.
		$P_\gamma = (4.5\pm1.0)10^{-5}$	Lobashov et al.1971 Sov.J.Nucl.Phys.13, 313	$(6\text{-}9)10^{-6}$	Eman & Tadic 1971 Phys.Rev. C4,661
	$5/2^+ \rightarrow 7/2^+$	$P_\gamma = (2.0\pm3.0)10^{-5}$	Boehm & Kankeleit 1968 Nucl.Phys. A109,457		
^{177}Hf	$9/2^+ \rightarrow 9/2^-$	$P_\gamma = (3.0\pm13.0)10^{-4}$	Boehm & Hauser 1960 Nucl.Phys. 14,615		

Nucleus	Transition	Experimental Value		Theoretical Value Cabibbo	
^{180}Hf	$8^- \rightarrow 6^+$	$P_\gamma = -(2.28 \pm 0.15) 10^{-3}$	Jenschke 1972 KFK-1739, Karlsruhe	$\sim(2) 10^{-3}$	Vogel 1971, Caltech Report, CALT-63-155
		$P_\gamma = -(2.0 \pm 0.4) 10^{-3}$	Kuphal 1972, Z. Phyzik 253,314		
		$A_\gamma = -(1.66 \pm 0.18) 10^{-2}$	Krane et al.1971 Phys.Rev. C4,1906		
	$8^- \rightarrow 8^+$	$P_\gamma = -(2.3 \pm 3) 10^{-2}$	Bock et al.1966 Phys.Lett. 22,316		
		$A_\gamma = -(19.4 \pm 9.2) 10^{-4}$	Krane et al.1972 Phys.Rev. C5,1663		
^{181}Ta	$5/2^+ \rightarrow 7/2^+$	$P_\gamma = -(6.1 \pm 0.7) 10^{-6}$	Lobashov et al.1971 Sov.J.Nucl.Phys. 13 313	$(3.5) 10^{-7}$	Desplanques 1975, Thesé, Université de Paris Sud.
		$P_\gamma = -(2.9 \pm 1.1) 10^{-6}$	Jenschke 1972 KFK-1739, Karlsruhe	$(3\text{-}11) 10^{-8}$	Gari et al.1971 Phys.Lett. 35B,19
^{182}W	$2^- \rightarrow 2^+$	$P_\gamma = -(2.5 \pm 4.0) 10^{-5}$	Lipson et al.1972 Phys.Rev. C5,932		
^{203}Tl	$3/2^+ \rightarrow 1/2^+$	$P_\gamma = (2.0 \pm 5.0) 10^{-6}$	Vanderleeden et al. 1972, Phys.Rev. C4,2218		
		$P_\gamma = (1.0 \pm 7.0) 10^{-6}$	Kuphal 1972, Z. Phyzik 253,314		
		$A_\gamma = (6.0 \pm 8.0) 10^{-5}$	Baker & Hamilton 1970 Phys.Lett. 31B,557		
		$A_\gamma = -(2.7 \pm 0.7) 10^{-4}$	Dydak et al. 1971 Phys.Lett. 37B,375		

Nucleus	Transition	Experimental Value		Theoretical Value Cabibbo
^{236}U	$\vec{n}$ fission	$A_{light} = (1.7\pm0.4)10^{-4}$	R.Wilson 1978 private communication*	
^{240}Pu	$\vec{n}$ fission	$A_{light} = -(4.8\pm0.8)10^{-4}$	R.Wilson 1978 private communication*	
		Electron-Nucleon (Neutral Current Only)		
^{2}H	$\vec{d+e} \rightarrow d+e$	$A/Q^2 = -(9.5\pm1.6)10^{-5}$	R. Taylor 1978 private communication	0
^{208}Bi	$3/2 \rightarrow 3/2$	$R = -(0.7\pm3.2)10^{-8}$	Lewis et al.1977, Phys.Rev.Lett. 39,795	0
	$3/2 \rightarrow 5/2$	$R = (2.7\pm4.7)10^{-8}$	Baird et al.1977 Phys.Rev.Lett. 39,798	0
		$R = (42\pm9)10^{-8}$	Barkov & Zolotorov 1978 JETP Lett. 26,379	

*Unpublished result from I.T.E.P. U.S.S.R.

Figure 1

Energy levels in ^{18}F (not to scale). Only those levels relevant to this experiment are shown.

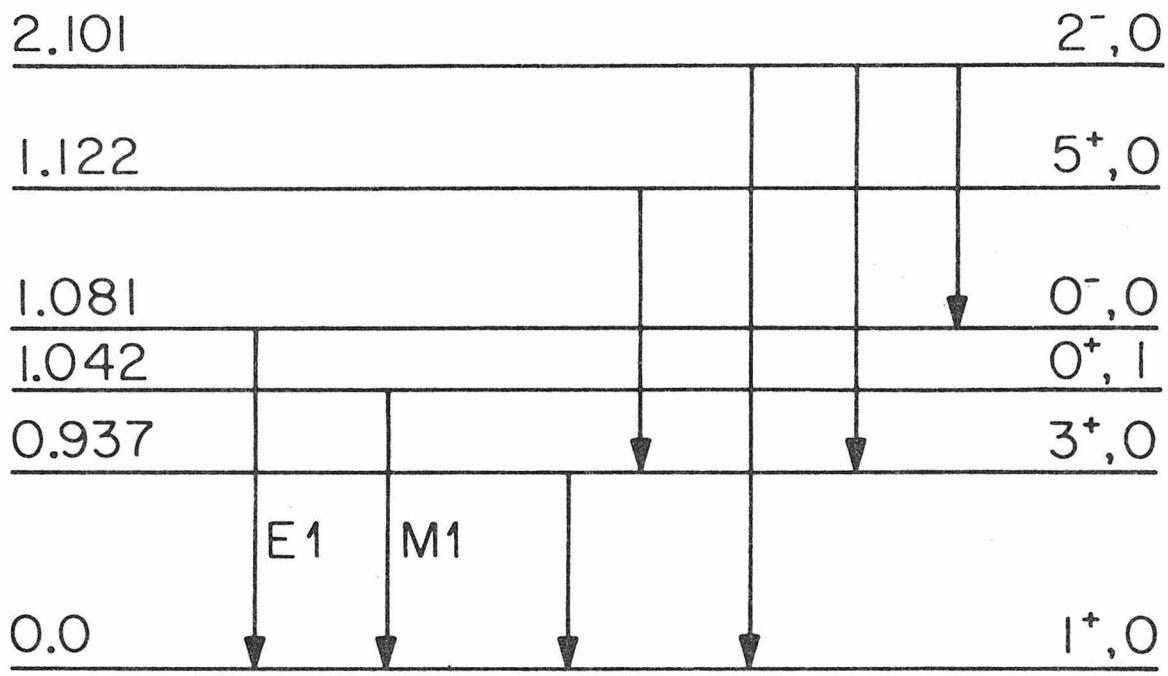
2.101
2⁻, 0
1.122
5⁺, 0
1.081
0⁻, 0
1.042
0⁺, 1
0.937
3⁺, 0
E1
M1
0.0
1⁺, 0
ENERGY (MeV)
Jᴾ, I

^{18}F

Figure 2

Sketch of the beam-line components as seen from the right side. The beam entered at A and passed through differential pumping canals B and D, which were separated by a region pumped by diffusion pump C. Needle-valve E admitted argon gas from F into the beam-fuzzing region, (D to K). Gate valve G was open during operation of the beam. Magnetic-focussing quadrupole H and magnetic steering dipoles I allowed adjustment of the focus and direction of the beam prior to its leaving the fuzzer through aperture K. Position J is the same point on both the upper half and the lower half of the drawing. The vacuum downstream of aperture K was provided by diffusion pump M, and gate valve N was normally open. In the event of a foil rupture, fast-acting vacuum valves O and P were triggered by ion gauges L and Q, respectively. The beam size was defined by aperture R. The beam then passed through cold trap S and aperture T to reach the target U (shown in greater detail in Figs. 3 and 4).

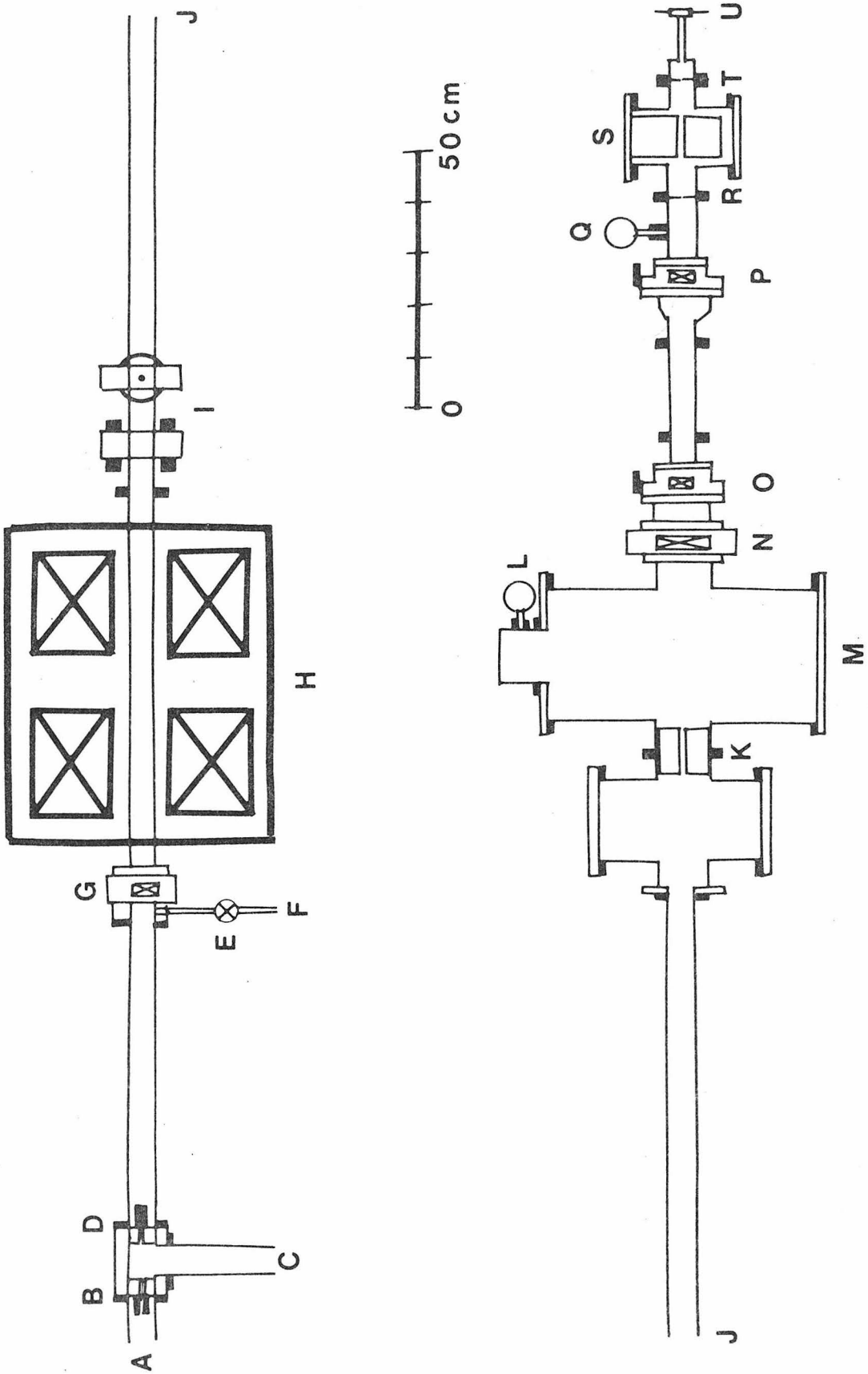
A
B
C
D
E
F
G
H
I
J
K
L
M
N
O
P
Q
R
S
T
U
0
50cm

Figure 3

Schematic layout of the water target system, shown in vertical section. The scale applies only to the left side of the drawing. The curvature of the nickel foil while supporting atmospheric pressure has been exaggerated.

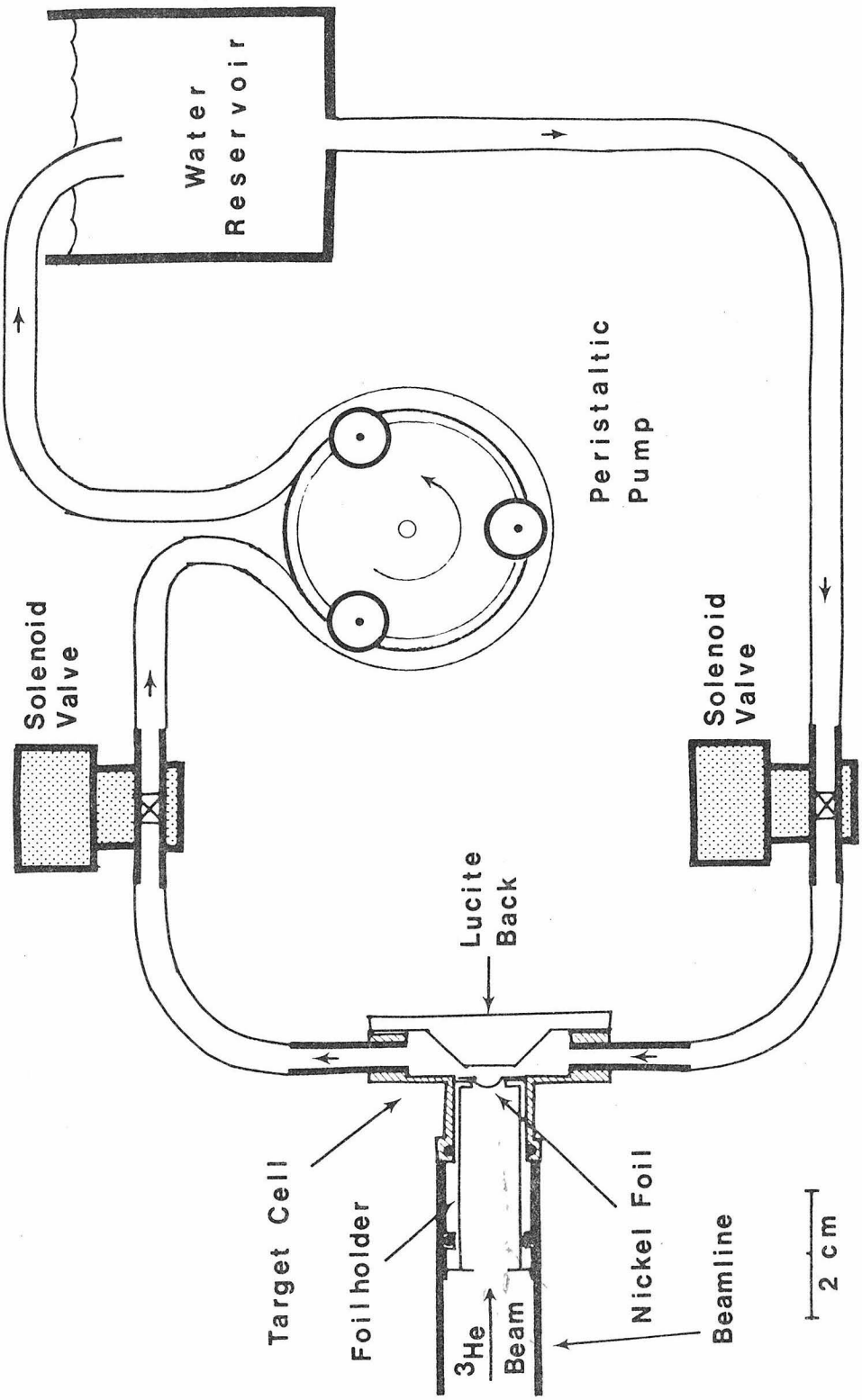
Water Reservoir
Peristaltic Pump
Solenoid Valve
Solenoid Valve
Lucite Back
Target Cell
Foilholder
^{3}He Beam
Nickel Foil
Beamline
2 cm

Figure 4

Schematic layout of polarimeters and target cell, shown in horizontal section.

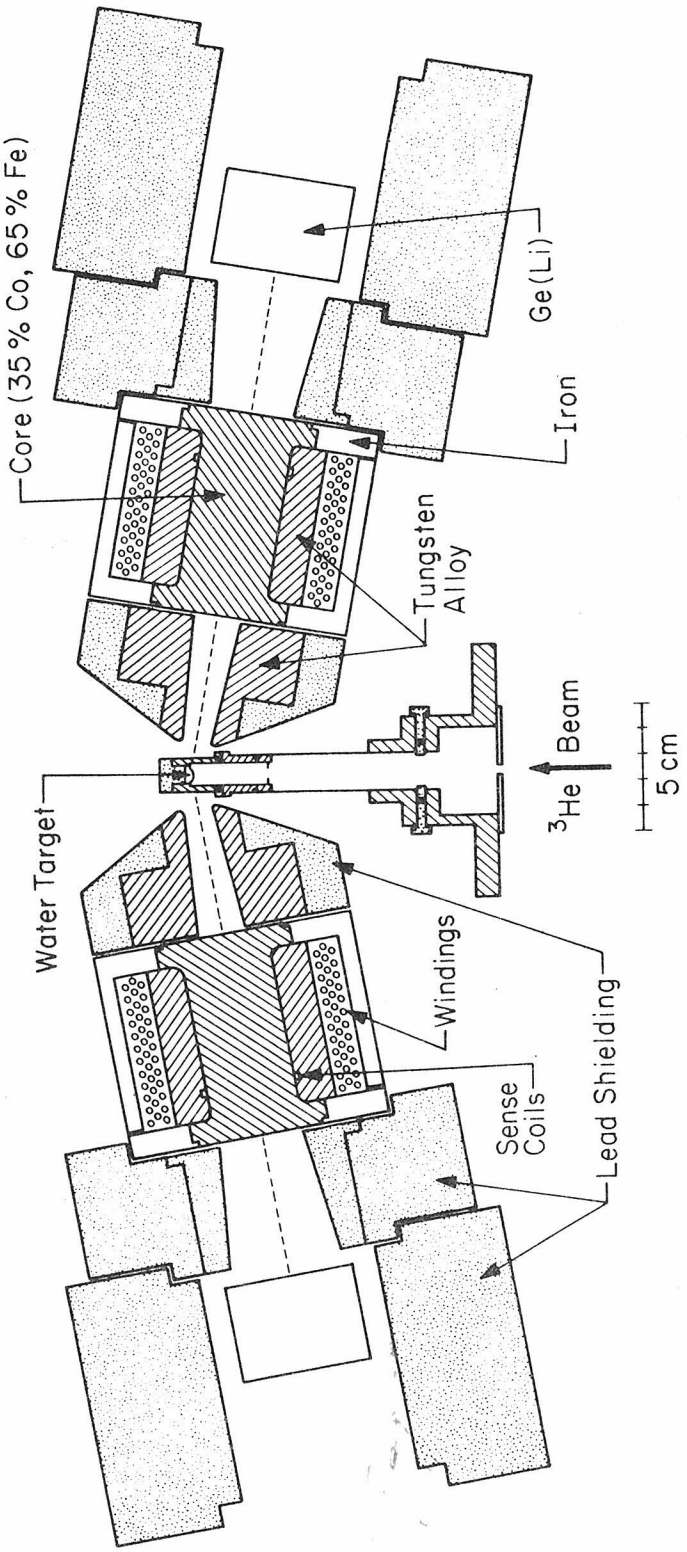
Core (35 % Co, 65 % Fe)
Ge(Li)
Iron
Tungsten Alloy
Water Target
^{3}He Beam
5 cm
Windings
Sense Coils
Lead Shielding

Figure 5

a) Timing relationships among voltage signals. The horizontal axis is not to scale, and the vertical scales are arbitrary.

b) Electronic circuitry block diagram.

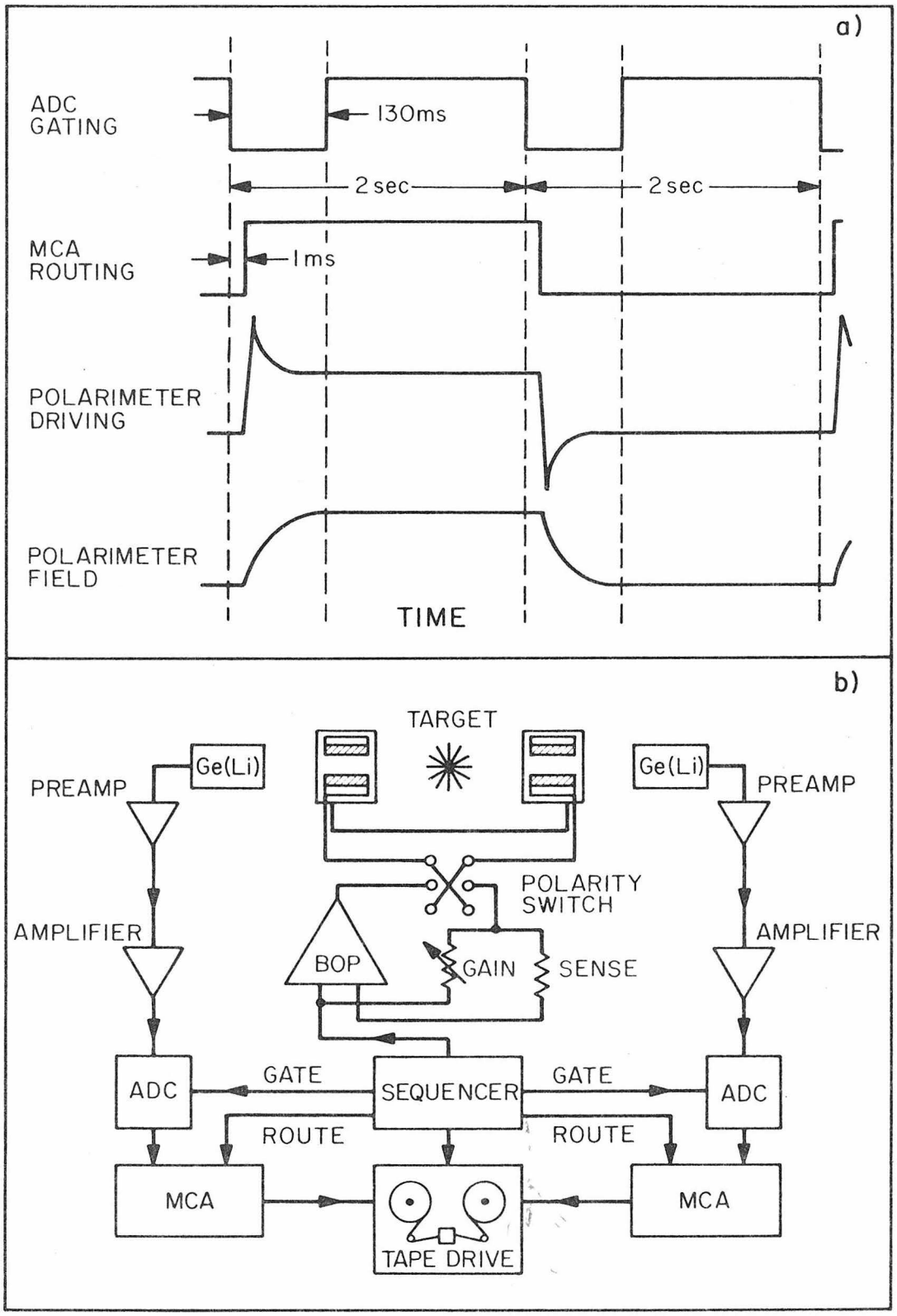
a)
ADC GATING
130ms
2 sec
2 sec
MCA ROUTING
1ms
POLARIMETER DRIVING
POLARIMETER FIELD
TIME
b)
TARGET
PREAMP
Ge(Li)
Ge(Li)
PREAMP
POLARITY SWITCH
AMPLIFIER
BOP
GAIN
SENSE
AMPLIFIER
ADC
GATE
SEQUENCER
GATE
ADC
ROUTE
ROUTE
MCA
MCA
TAPE DRIVE

Figure 6

Stray horizontal magnetic field measured along beam line. Shown here are differences between the plus and minus routes; a) without compensating coils; c), e), and g) with three different versions of compensating coils described in the text. The product of field times the distance from the target (chosen as origin) is given in b), d), f) and h) for each of the four cases, respectively. The areas are arrived at by assuming that the fields far upstream decay as $1/x^3$. The dashed curves are the data curves multiplied by 10; the dotted curves the data multiplied by 100.

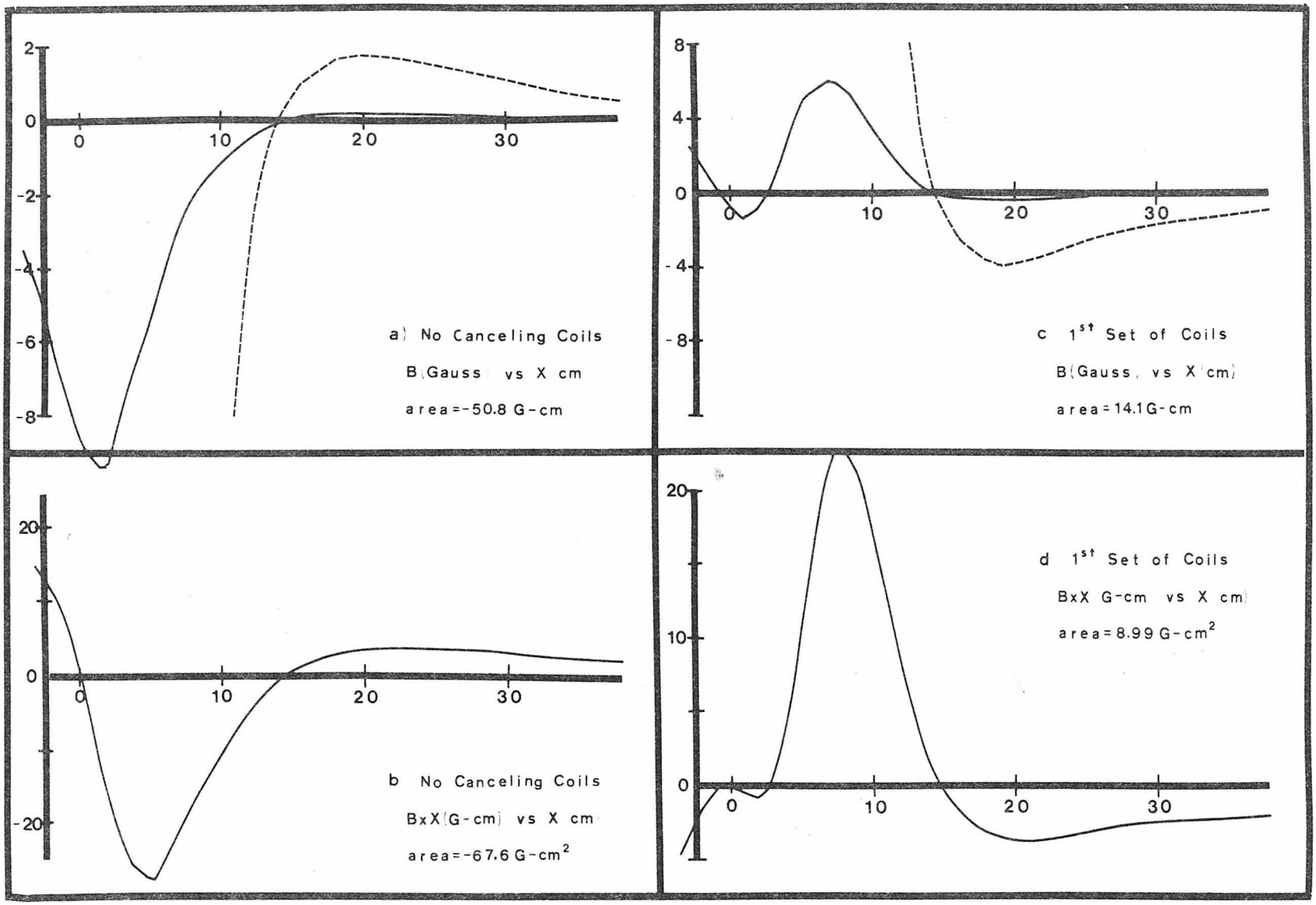
2
0
-2
-4
-6
-8
0
10
20
30
a) No Canceling Coils
B(Gauss vs X cm
area=-50.8 G-cm
8
4
0
-4
-8
0
10
20
30
c 1st Set of Coils
B(Gauss, vs X cm)
area=14.1G-cm
20
0
-20
0
10
20
30
b No Canceling Coils
BxX(G-cm) vs X cm
area=-67.6 G-cm²
20
10
0
0
10
20
30
d 1st Set of Coils
BxX G-cm vs X cm
area=8.99 G-cm²

Figure 6 - continued

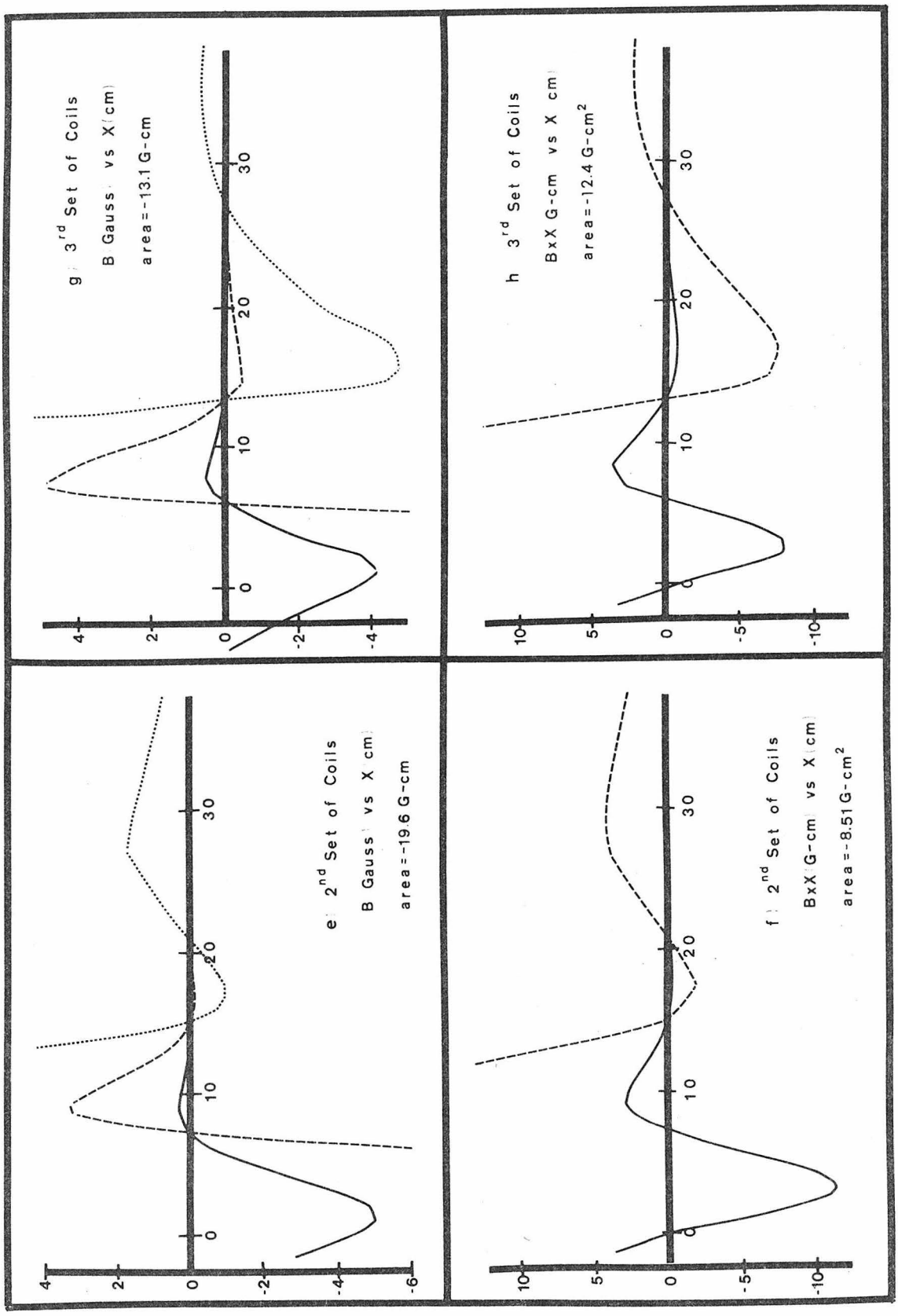
e) 2nd Set of Coils
B Gauss vs X cm
area=-19.6 G-cm
f) 2nd Set of Coils
BxX G-cm vs X cm
area=-8.51 G-cm²
g) 3rd Set of Coils
B Gauss vs X cm
area=-13.1 G-cm
h) 3rd Set of Coils
BxX G-cm vs X cm
area=-12.4 G-cm²

Figure 7

Typical pulse-height spectrum. The ten spectral regions for which asymmetries were determined are shaded.

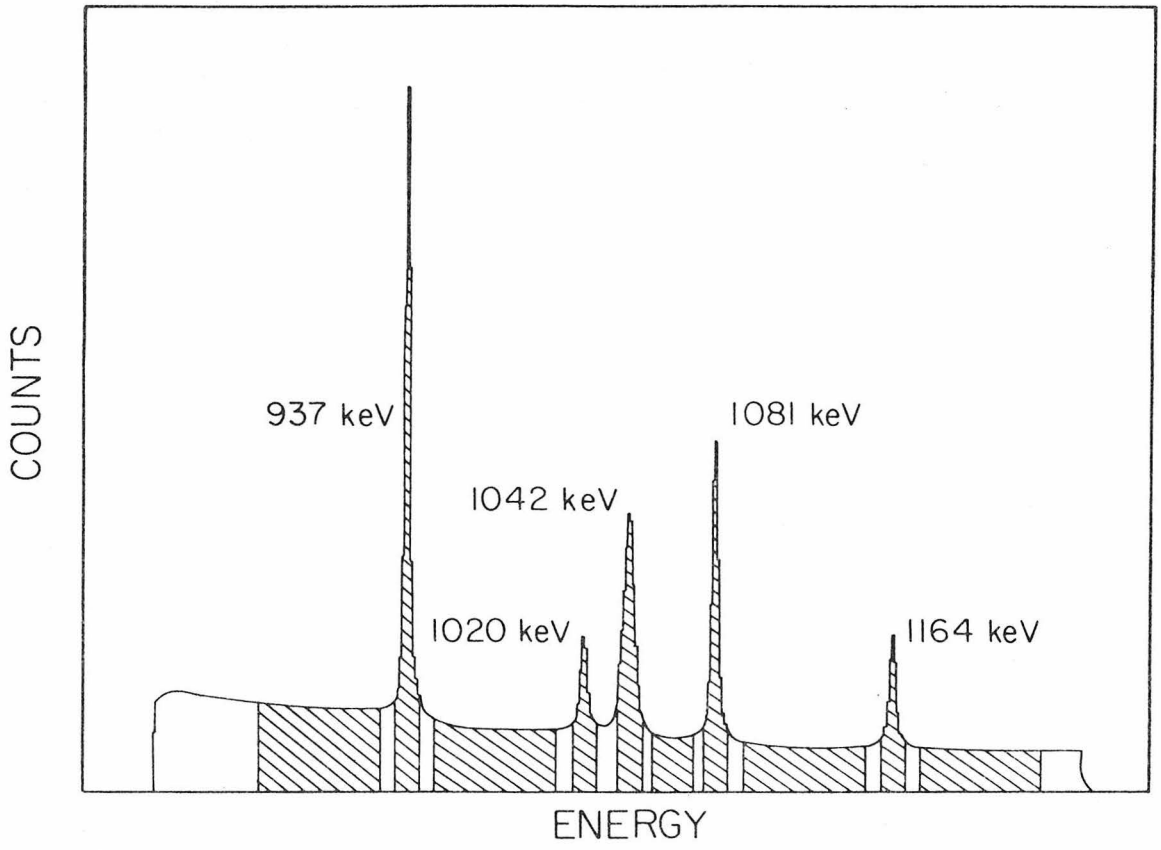
COUNTS
937 keV
1042 keV
1081 keV
1020 keV
1164 keV
ENERGY

Figure 8

Asymmetry during each data-taking session for each of the ten spectral regions. The sessions are listed and numbered in Table I. 8a) shows the asymmetries of the five peak regions for the portions of the sessions while the polarimeter-lead polarity switch was in the "normal" position. 8b) shows the asymmetries of the five background regions (labeled B1 through B5 in order of increasing energy) under the same condition as 8a). 8c) and d) give the asymmetries of the peak and background regions, respectively, while the polarity switch was in the "reverse" position. Not all sessions contained data for both positions.

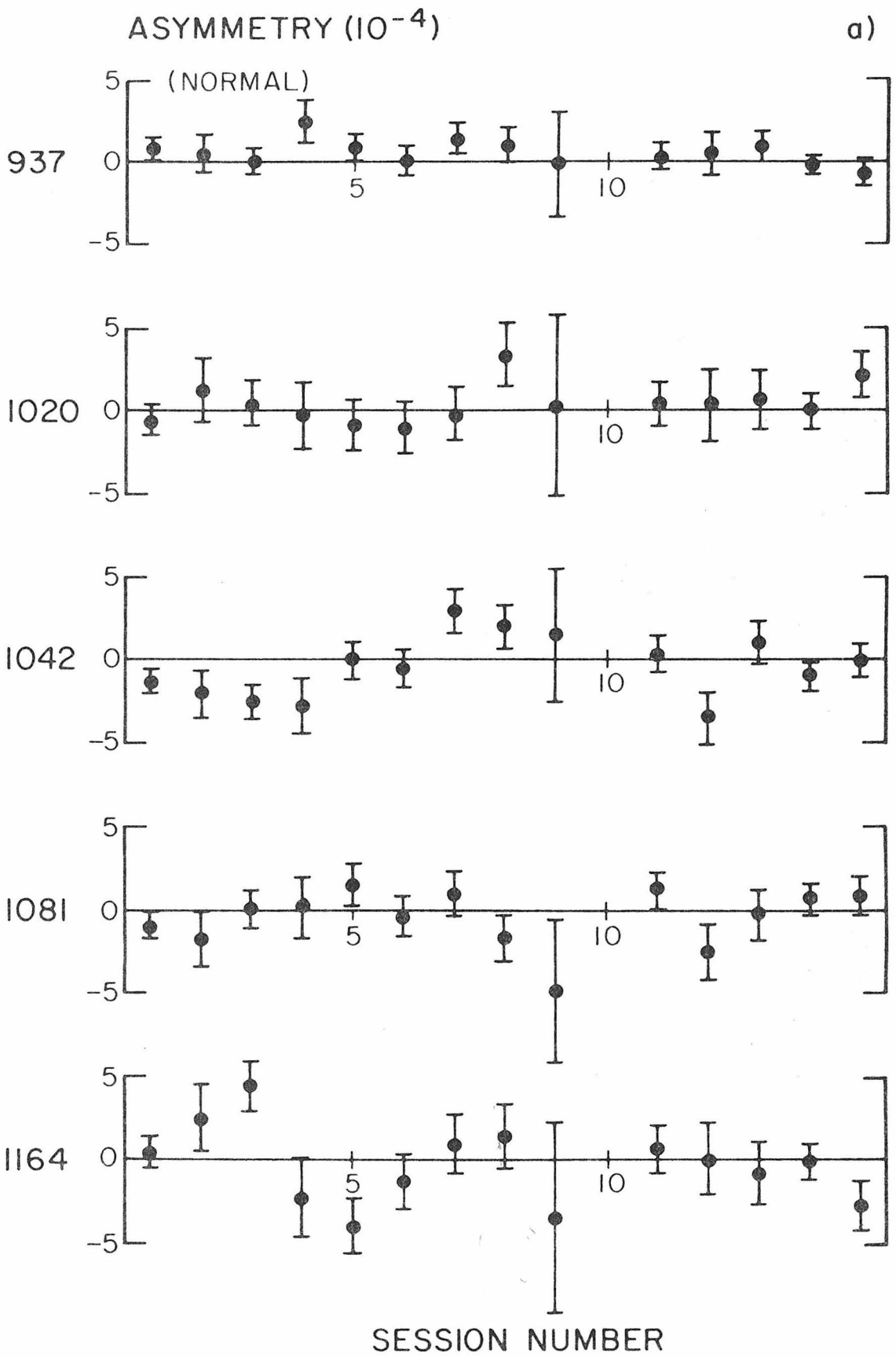
ASYMMETRY (10^{-4})
a)
(NORMAL)
937
1020
1042
1081
1164
5
0
-5
5
10
SESSION NUMBER

Figure 8 - continued

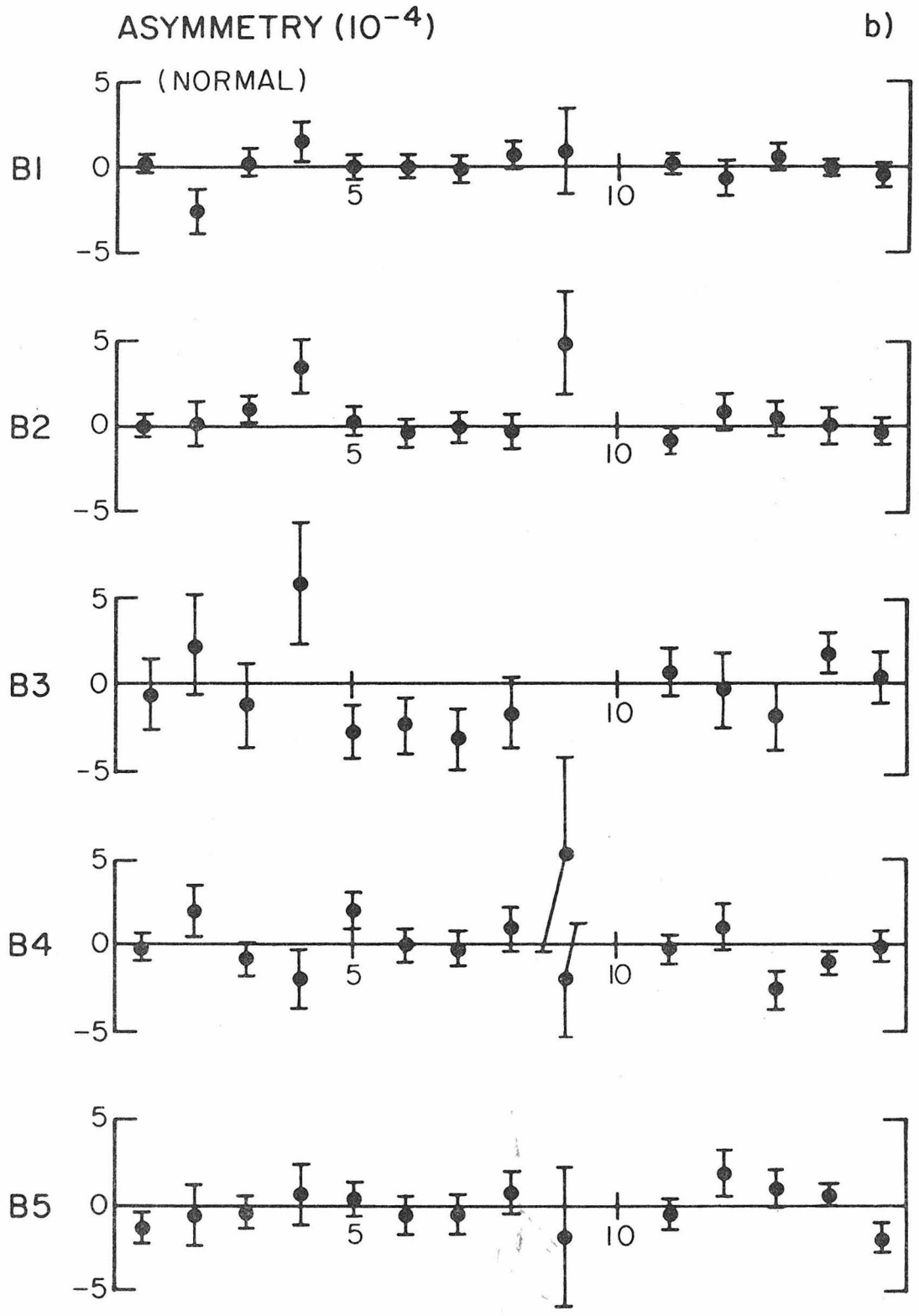
ASYMMETRY (10^{-4})
b)
(NORMAL)
B1
B2
B3
B4
B5
5
0
-5
5
10
SESSION NUMBER

Figure 8 - continued

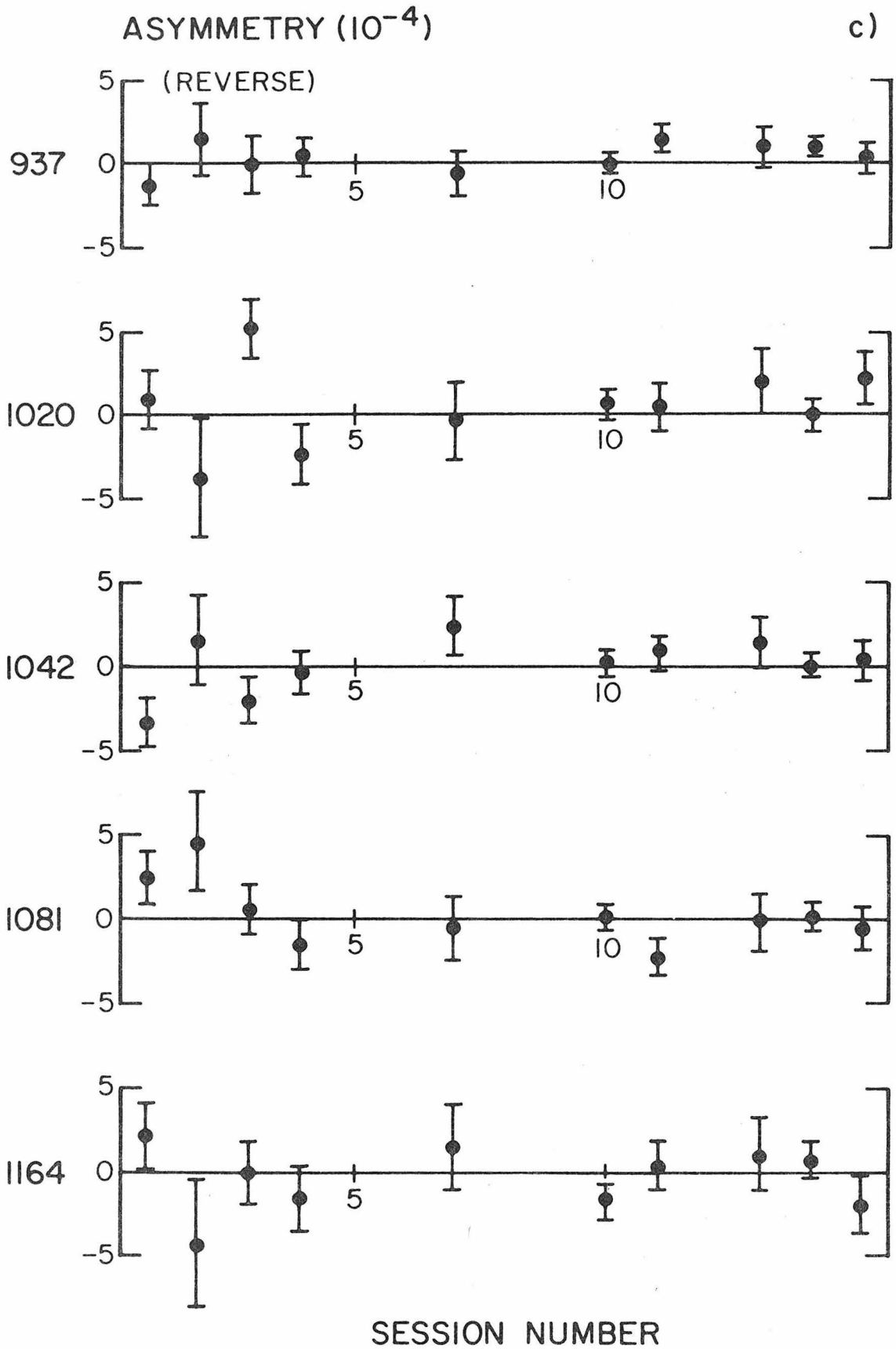
ASYMMETRY (10^{-4})
c)
(REVERSE)
937
1020
1042
1081
1164
5
0
-5
5
10
SESSION NUMBER

Figure 8 - continued

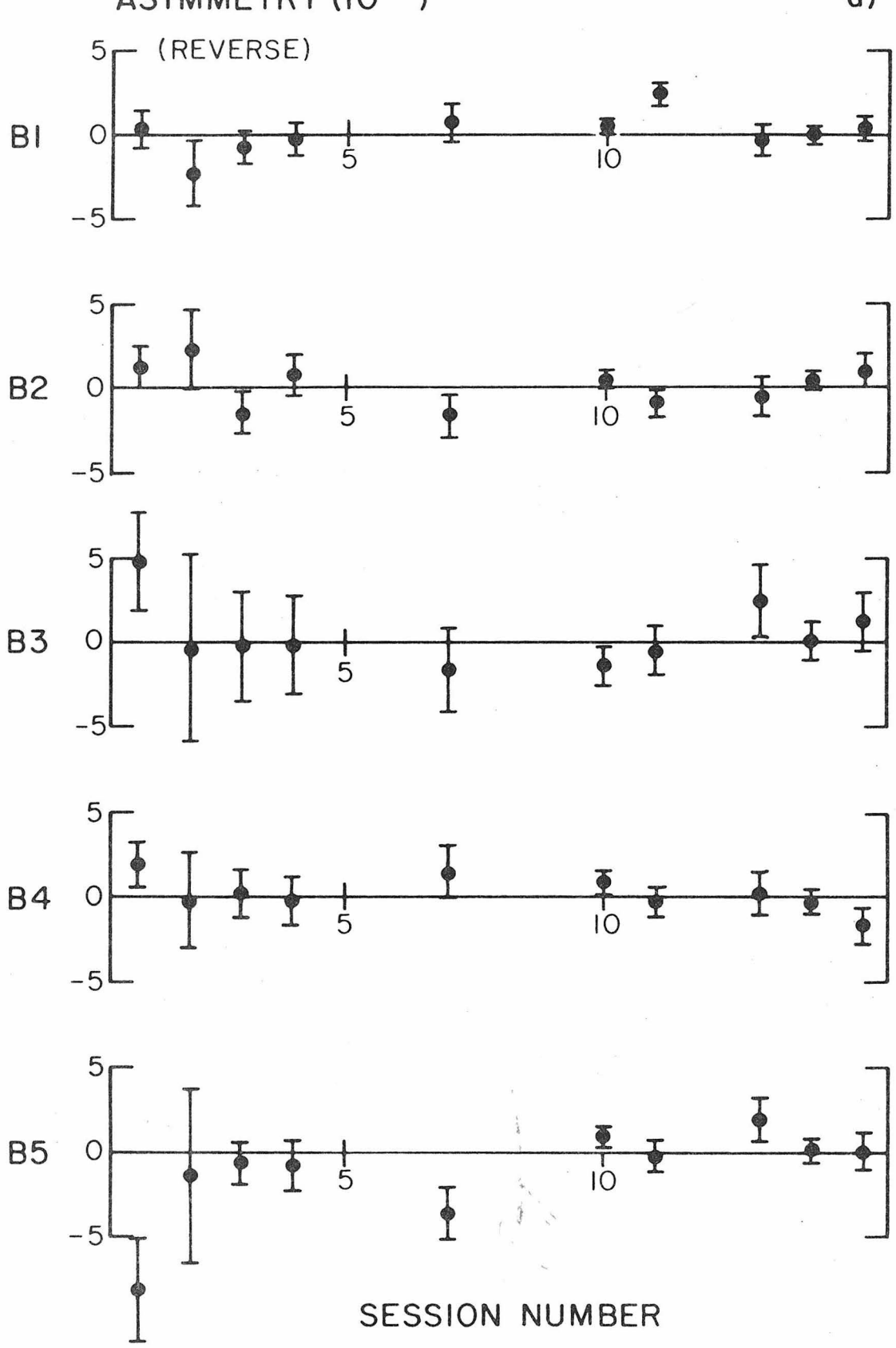
ASYMMETRY (10^{-4})
d)
(REVERSE)
B1
B2
B3
B4
B5
5
0
-5
5
10
SESSION NUMBER

Figure 9

Summed asymmetries for the five peak regions (closed circles) and the five background regions (open circles). Graphs are given for the "normal" polarimeter-lead polarity switch position, for the "reverse" position, and for the total of both positions. In addition, the reduced chi-squares of the results of the individual data-taking sessions about the means shown here are graphed at the bottom of the figure. The right-hand scales of these graphs give the percentage probabilities of obtaining an equal-or-larger reduced chi-square from a Gaussian distribution for the appropriate number of degrees of freedom (14,11,24)

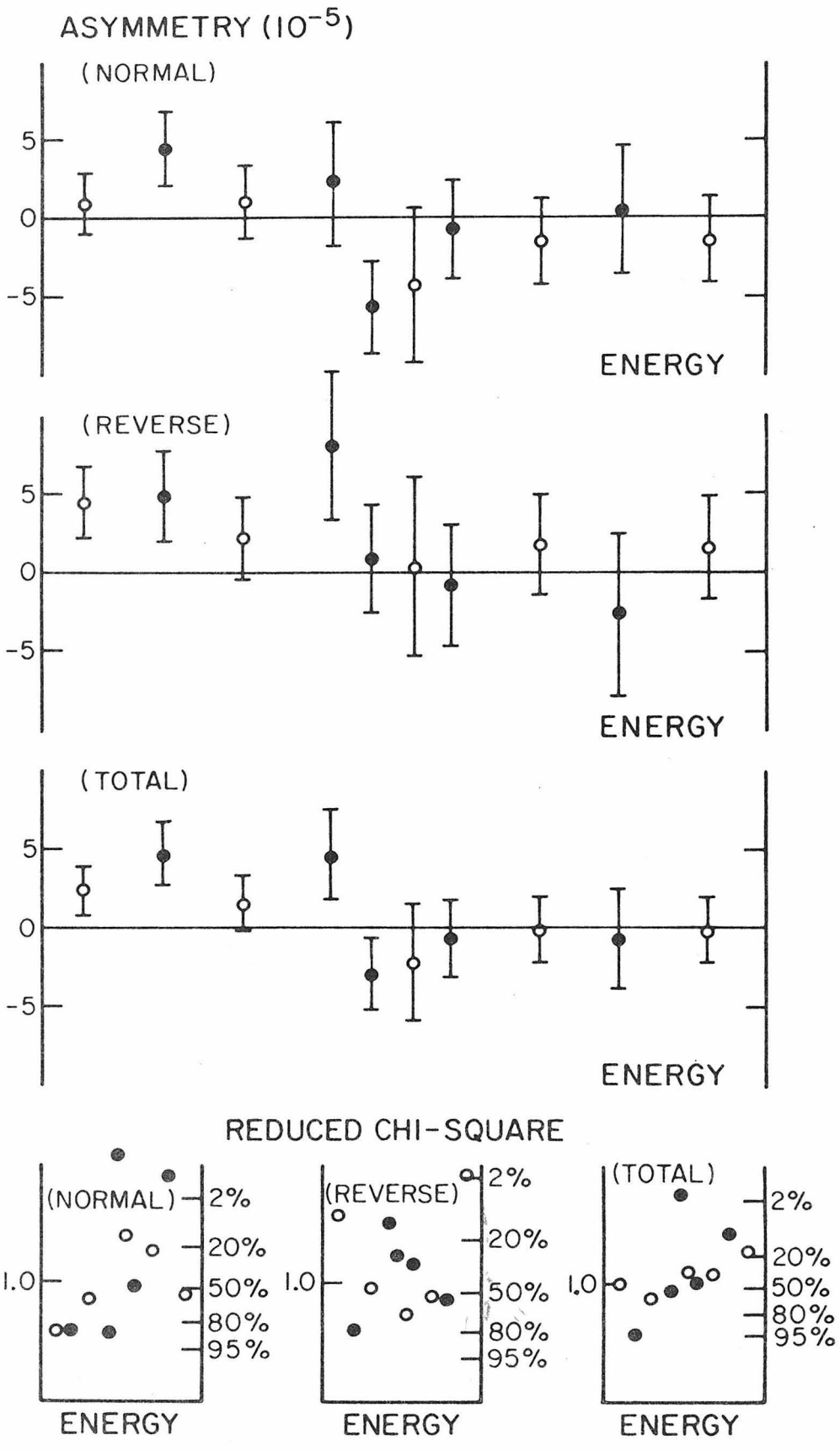
ASYMMETRY (10^{-5})
(NORMAL)
5
0
-5
ENERGY
(REVERSE)
5
0
-5
ENERGY
(TOTAL)
5
0
-5
ENERGY
REDUCED CHI-SQUARE
(NORMAL)
2%
20%
50%
80%
95%
1.0
ENERGY
(REVERSE)
2%
20%
50%
80%
95%
1.0
ENERGY
(TOTAL)
2%
20%
50%
80%
95%
1.0
ENERGY

Figure 10

Vertical section of the experimental setup for the analyzing power measurement.

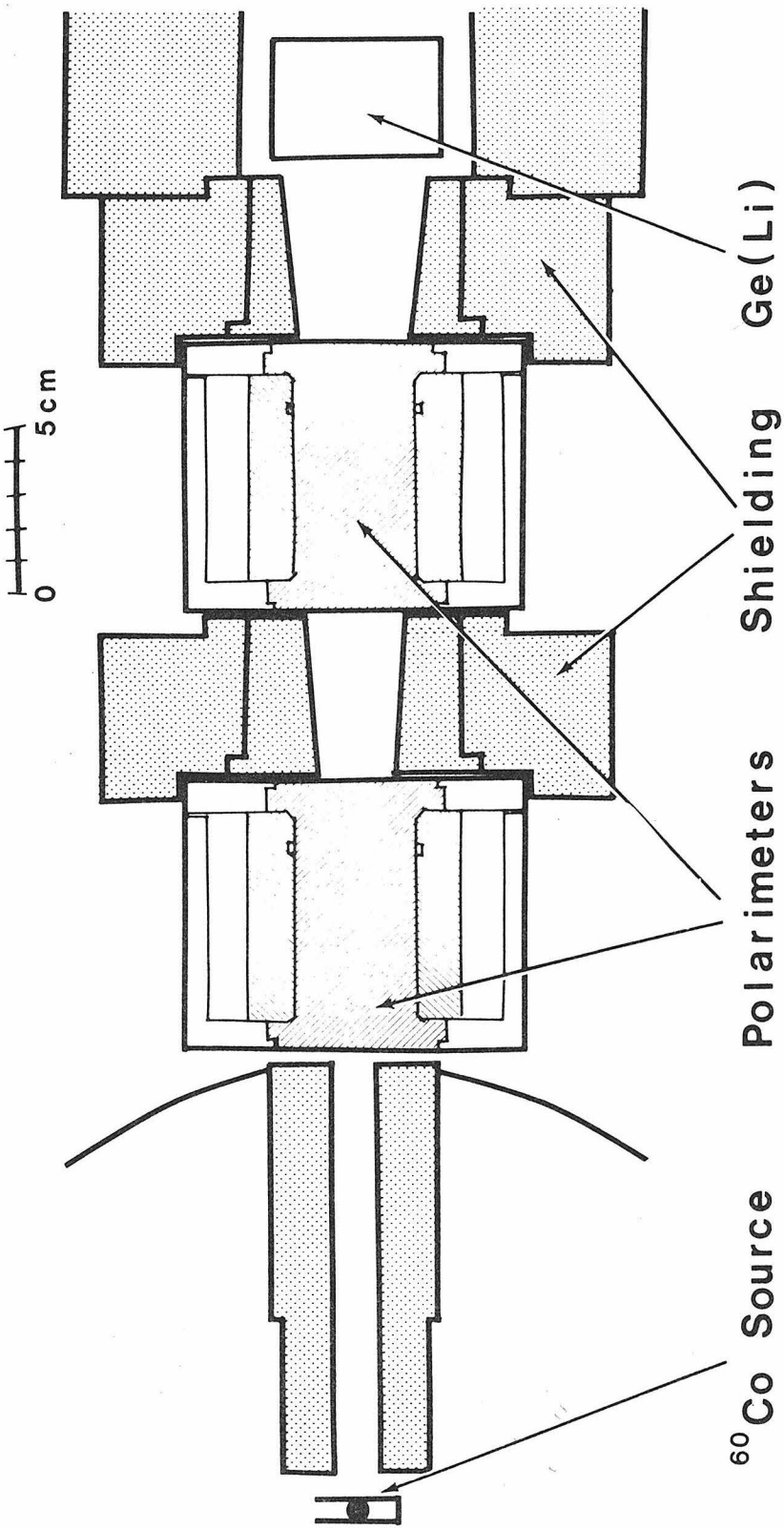
Ge(Li)
Shielding
Polarimeters
^{60}Co Source
0
5 cm

Figure 11

Asymmetries of the peak regions (closed circles) and background regions (open circles) during the analyzing power measurement. The uppermost graph is for the runs taken with a pulse generator set to give a peak at higher energy than the 1332 keV peak. The graph below it is for the runs with the pulser set to produce a peak below the 1173 keV peak. The dotted lines are linear fits to the background regions made independently for the two pulser positions. The solid lines are a linear fit to the background regions for both pulser positions treated simultaneously. The crosses show the asymmetries of the ^{60}Co peaks after background subtraction and correction for the null shift.

At the bottom of the figure are given the reduced chi-squares of the runs about the results in the upper two graphs. The right-hand scales of the reduced chi-square graphs give the percentage probability of obtaining an equal-or-larger reduced chi-square from a Gaussian distribution for the appropriate number of degrees of freedom (8 and 5).

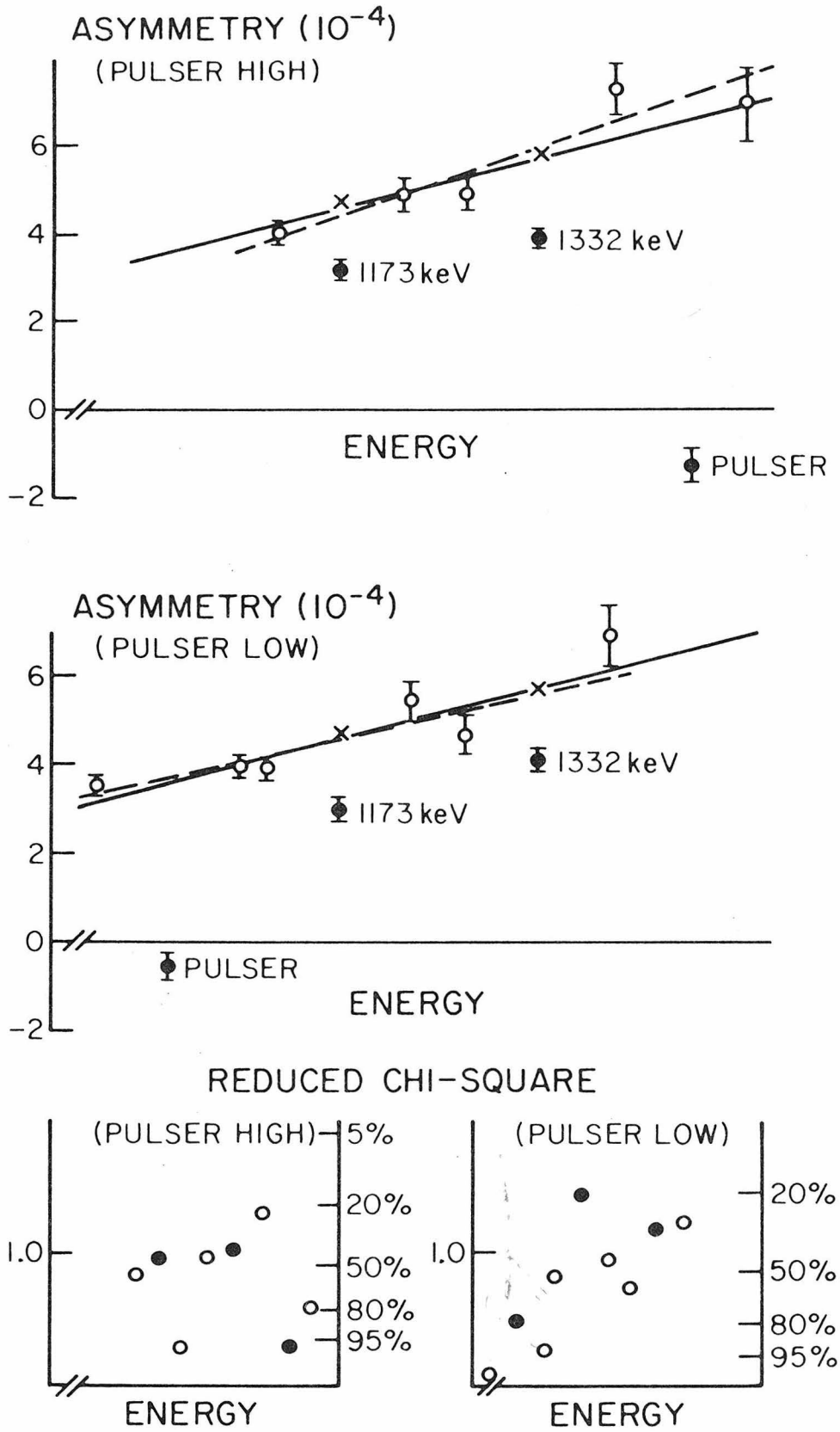
ASYMMETRY (10^{-4})
(PULSER HIGH)
6
4
2
0
-2
1332 keV
1173 keV
ENERGY
PULSER
ASYMMETRY (10^{-4})
(PULSER LOW)
6
4
2
0
-2
1332 keV
1173 keV
PULSER
ENERGY
REDUCED CHI-SQUARE
(PULSER HIGH)
5%
20%
50%
80%
95%
1.0
ENERGY
(PULSER LOW)
20%
50%
80%
95%
1.0
ENERGY

Figure 12

Angular distributions of the 937 keV and 184 keV gamma rays from ^{18}F. 12a) shows the de-excitation gamma ray of the 937 keV state $(3^+,0)$ to the ground state $(1^+,0)$ when the state is created in a thick target by a 4.0 MeV ^3He beam traversing a 750 nanometer nickel foil. The solid line is a fourth-order, even-Legendre-polynomial fit to the data. Error bars are smaller than the points. 12b) shows the de-excitation of the 1122 keV state $(5^+,0)$ to the 937 keV state $(3^+,0)$ under the same conditions as 12a). The solid line is again an even Legendre polynomial fit up to fourth order. 12c) and d) are the same as a) and b), respectively, except that the beam traversed a 1000 nanometer foil instead of the 750 nanometer foil before reaching the oxygen target.

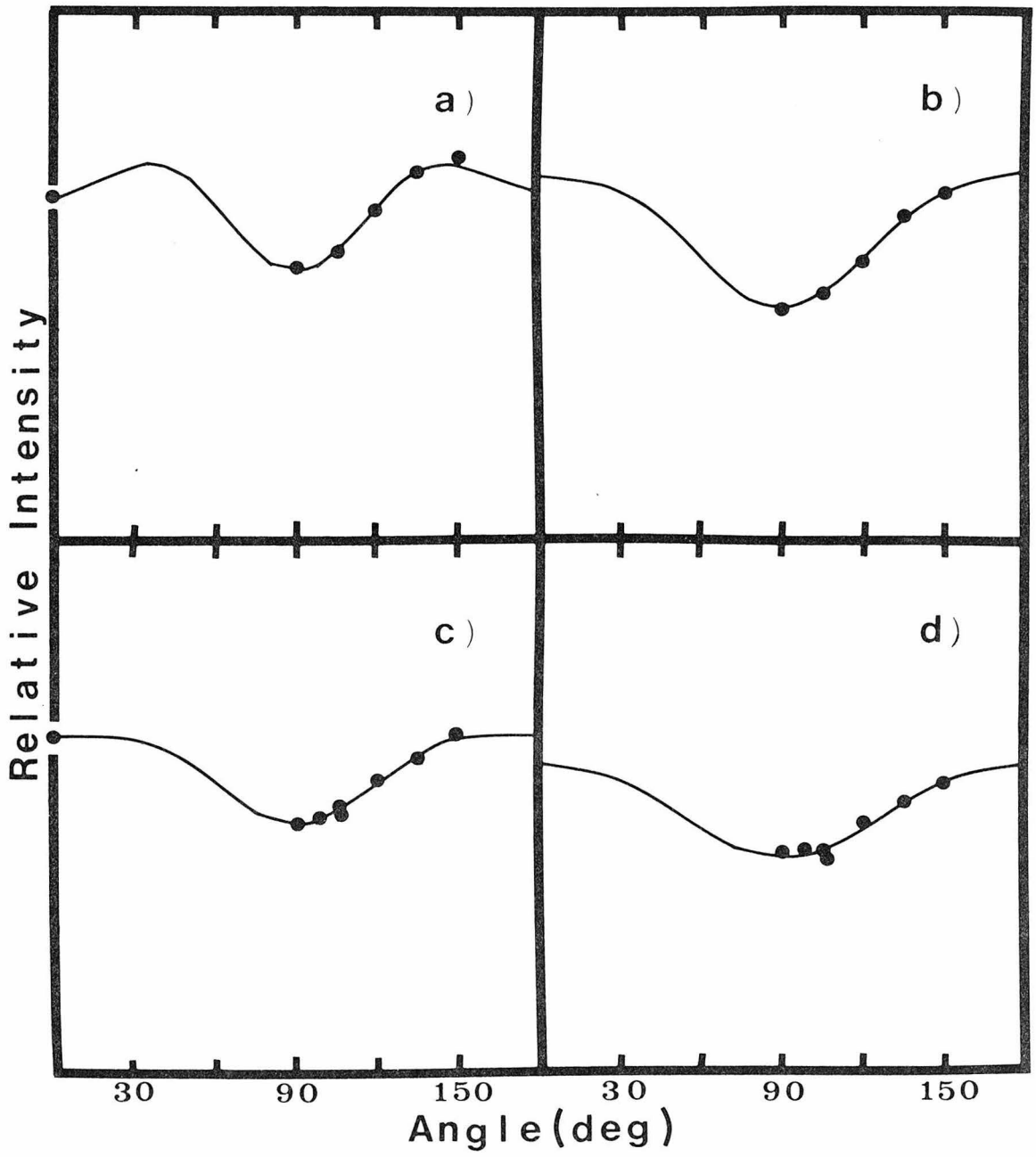
a)
b)
c)
d)
Relative Intensity
30
90
150
30
90
150
Angle(deg)